

Chapter-5

Tungstate Based Double Perovskite Phosphors: Role of Rare Earths (Tb^{3+} and Ho^{3+}) on the Luminescence Properties

Highlights

Part-I

This section discusses the structural and luminescence optimization in terbium activated tungstate double perovskite Ca_3WO_6 . A detailed structural study of the phosphor under study were carried out in terms of XRD, SEM, EDAX and FTIR characterization techniques. The PL study's findings suggesting an efficient green emitting perovskite phosphor with excellent CIE color coordinates. Moreover, in TL, the phosphor explored for their wide investigation aspects, such as effect of doping concentration, effect of beta radiation dose, and most important the TL fading.

Part-II

In this section, a detail of investigation on the Ho^{3+} single doped Ca_3WO_6 double perovskite is discussed. The series of the holmium activated tungstate phosphors were prepared via the combustion synthesis. The phosphor studied extensively for their structural characterization, including XRD, SEM, EDAX and FTIR. An interesting phenomenon of up-conversion luminescence was observed in addition with down-conversion luminescence from Ho^{3+} doped Ca_3WO_6 phosphor. A high thermal stability of the phosphor was found from temperature dependent PL. Moreover, the TL display is also found to be interesting between undoped and doped Ca_3WO_6 . In TL, effect of doping, effect of ionizing dose and effect of different heating rates on TL intensity were investigated and discussed.

5.1 Introduction

In recent times, extensive research has been carried out to explore materials doped with rare earth elements due to their appreciated technological applications, including in LEDs and displays. Trivalent lanthanides with electron reach $4f^n$ ($n=0-14$) electronic configuration and abundant energy levels have become very popular in areas of illumination technology and radiation dosimetry [1,2]. The emission of visible light is ascribed to electronic transitions arising from the $4f$ states of rare earth ions. A potential light-emitting material, also known as phosphor material, comprises the host material activated with luminescence activators. There has been significant research on the phosphors activated by rare earth elements was carried out. Phosphors doped with elements like europium (Eu^{3+}), terbium (Tb^{3+}), and cerium (Ce^{3+}) are extensively studied for applications in lighting devices and displays. Neodymium (Nd^{3+}) and ytterbium (Yb^{3+}) are very promising for laser technology, while gadolinium (Gd^{3+}) emitted UV light is applied in medical purposes [3-5]. Consequently, the demand for the development of phosphor materials capable of emitting visible light was never-ending.

Plenty of research has been done on rare earth activated and co-activated phosphors for their luminescence characterization. In addition, several studies on the perovskites that has been doped with rare earths was also found, during literature survey. Previously, $\text{Ca}_9\text{MgLi}(\text{PO}_4)_7:\text{Dy}^{3+}$ [6], $\text{La}_3\text{Br}(\text{SiS}_4)_2:\text{Ce}^{3+}/\text{Eu}^{2+}$ [7], $\text{Ca}_3\text{M}_2\text{Ge}_3\text{O}_{12}:\text{Mn}^{2+},\text{Mn}^{4+}$ ($\text{M} = \text{Al}, \text{Ga}$) [8], $(\text{Sr},\text{Ba})_2\text{SiO}_4:\text{Tb}^{3+}/\text{Eu}^{2+}$ [9] phosphors having different rare earths were reported for their potential applications in white light emitting diodes (WLEDs). A europium activated CaIn_2O_4 phosphor shows excellent color tunability [10], whereas, $\text{Eu}^{3+}:\text{LaF}_3$ [11] is reported for their biological applications. The phosphors that exhibited persistent/long-lasting luminescence were also found in the literature, such as $\text{CdSiO}_3:\text{Tb}^{3+}$ [12] and $\text{Sr}_2\text{SnO}_4:\text{Tm}^{3+}$ [13]. An up-converting phosphors $\text{SrGd}_2(\text{WO}_4)_2(\text{MoO}_4)_2:\text{Yb}^{3+}/\text{Ho}^{3+}$ [14], $\text{Ca}_3\text{WO}_6:\text{Yb}^{3+}/\text{Ho}^{3+}$ [15], $\text{Y}_2\text{Ti}_2\text{O}_7:\text{Er}^{3+}$ [16] are also be an subject of luminescence investigation. Moreover, the thermoluminescence properties of the phosphors doped with lanthanides also received huge interest due to its personal, medicinal, accidental, and radiation dosimetry applications. Several rare earth activated phosphors, including, $\text{Ba}_2\text{ZnSi}_2\text{O}_7:\text{Dy}^{3+}$ [17], $\text{Zn}(\text{BO}_2)_2:\text{Tb}^{3+}$ [18], $\text{KSr}_4(\text{BO}_3)_3:\text{Ce}$ [19] were reported for their excellent display of thermoluminescence. Unfortunately, the double perovskites received less attention for TL characterization, as per the concerned literature. Very few perovskites were reported for their TL properties.

5.2 Experimental and Characterizations

5.2.1 Phosphor Preparation

Two series of Ca_3WO_6 double perovskites, one is doped with Tb^{3+} and other is doped with Ho^{3+} were prepared via the combustion synthesis. The concentration of Tb^{3+} is taken from 0.5 mol% to 2.5 mol%, whereas the Ho^{3+} concentration is taken as 1 mol% to 5 mol%. To prepared the phosphors, AR grade CaCO_3 (99.9 %), WO_6 (99.9%), Tb_4O_7 (99.9%), and Ho_2O_3 (99.9%) of loba-chemi suppliers are taken in stoichiometric and mixed with urea (15% weight of the entire mix, 99%). Later, these mixtures were grounded and calcinated at 1200°C for 6 hr in muffle furnace, and then allowed to natural cool up to room-temperature. The fine white powder was obtained as a final product, and was grounded further for the characterizations.

5.2.2 Characterizations

All the prepared phosphors were first examined by XRD. The XRD were recorded via a D8 Bruker advance X-ray diffractometer within 20° to 70° angle of diffraction with step of $0.02^\circ/\text{s}$. To visualize the phosphor surface, the SEM characterization is carried out. The FTIR spectra of the studied phosphors were recorded via a Jasco FTIR-4100 spectrometer in transmittance mode, by using the KBr pellet technique. The PL excitation and emission spectra of the phosphors under study were recorded a Shimadzu Spectro-fluorophotometer, where a xenon flash lamp used as excitation source. Furthermore, the TL of all the phosphors were recorded after the irradiation by beta rays using ^{90}Sr beta source. The TL measurements of $\text{Ca}_3\text{WO}_6:\text{Tb}^{3+}$ phosphors were recorded via the NUCLEONIX TL READER of type TL1009, whereas, the TL measurements of $\text{Ca}_3\text{WO}_6:\text{Ho}^{3+}$ phosphors were done by using Risø TL/OSL reader DA 15 (Bøtter-Jensen et al., 2003) instrument.

Part-I

Luminescence Studies of $\text{Ca}_3\text{WO}_6:\text{Tb}^{3+}$

The following section describes the luminescence studies of synthesized phosphor namely $\text{Ca}_3\text{WO}_6:\text{Tb}^{3+}$, the obtained results, and characterizations.

5.3 Results and Discussion

5.3.1 XRD Studies

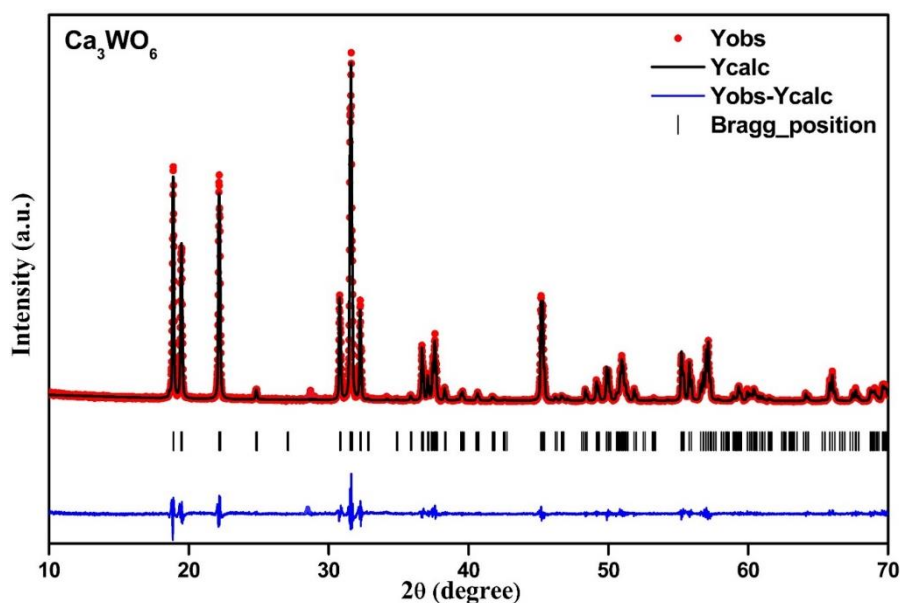
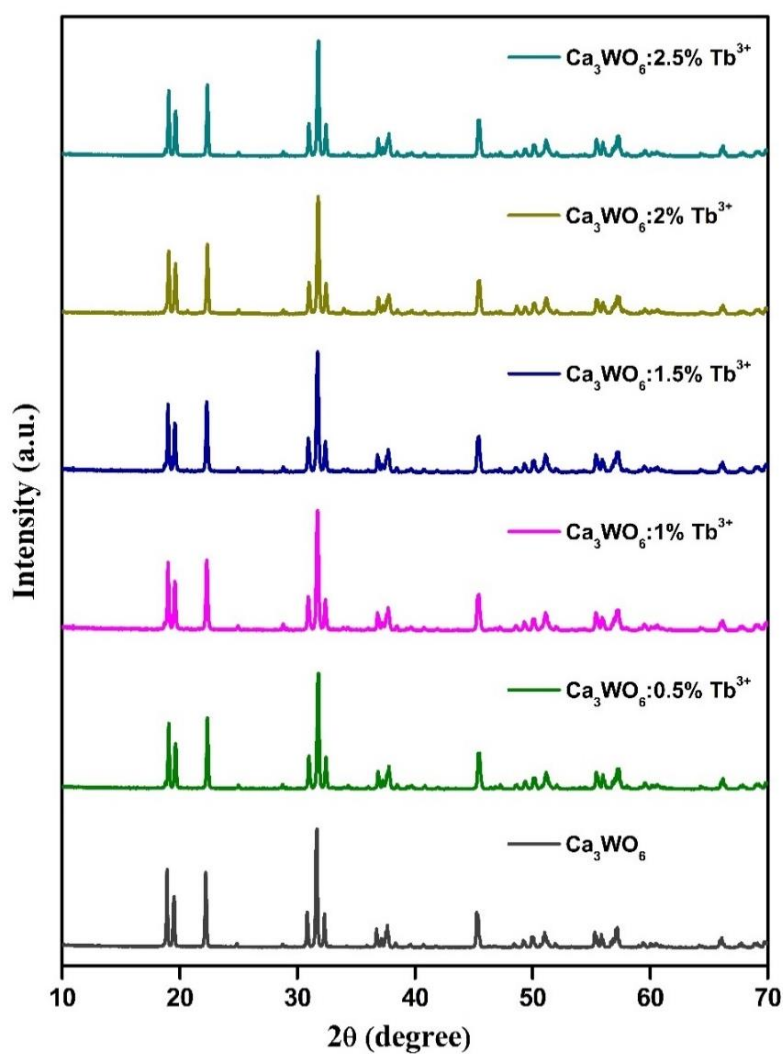


Figure 5.1. Rietveld refined XRD pattern of Ca_3WO_6 .

Figure 5.1 present the results of the Rietveld refined powder X-ray diffraction analysis conducted on pure Ca_3WO_6 phosphor using the Fullprof Suite computer program. The powder XRD pattern of Ca_3WO_6 material exhibit sharp diffraction peaks, indicating a high level of crystallinity. All visible diffraction peaks in diffraction pattern were crystallized to a pure monoclinic structure. All Ca_3WO_6 double perovskite phosphors, including Tb^{3+} doped and undoped samples exhibited a pure monoclinic crystalline structure with a P 21/c symmetry [20,21]. The lattice parameters obtained through Rietveld refinement analysis of the XRD pattern for undoped Ca_3WO_6 are presented in Table 5.1.

Figure 5.2 illustrate the X-ray diffraction (XRD) patterns of both pure and Tb^{3+} doped Ca_3WO_6 phosphors. The XRD patterns for all investigated compositions exhibited observable similarity, indicating that they all are crystalline to a pure monoclinic crystal structure. Particularly, no significant change in the XRD patterns upon Tb^{3+} dopants introduction was observed, as per identical XRD patterns. Moreover, no significant change in the cell volume is observed upon increased concentration of Tb^{3+} .

Formula	Ca₃WO₆
Radiation	Cu K α
2θ range	10-70°
Symmetry	Monoclinic
Space group	P 21/c
a (Å)	5.54
b (Å)	5.79
c (Å)	7.98
β	90.20°
R_p	12.5
R_{pw}	16.7
χ^2	1.95
V (Å³)	256.72

Table 5.1. Refined parameters of undoped Ca₃WO₆.Figure 5.2. XRD patterns of Ca₃WO₆: x mol% Tb³⁺ (x= 0-2.5) phosphors.

The identical XRD patterns of all studied compositions suggest the successful incorporation of Tb^{3+} ions into the host matrix without perturbing the original crystal structure. Minor fluctuations in the intensity counts of the diffraction peaks in the XRD pattern may be due to the substitution of dopant ions and/or due to the non-reactive part of the host material. To justify the substitution of Tb^{3+} ions, the concept of ionic radii of the substituted and substituting ions was taken into account. The Tb^{3+} ions with an ionic radius of 0.923 Å and a coordination number (CN) of 6, are most likely to replace Ca^{2+} ions, which have an ionic radius of 1.00 Å and a CN of 6, in the host lattice [22]. To validate the above-mentioned statement on ion substitution, Pires and Davolos proposed an acceptable percentage difference (D_r), and that should not exceed 30% [23]. To confirm the site substitution, we calculated the percentage difference using the formula 3.1 (section 3.3.1). The calculated D_r value for the substitution of Tb^{3+} dopant at Ca^{2+} site was obtained to be 7.7% [24]. This outcome provides enough evidence that Tb^{3+} ions are certainly replacing Ca^{2+} ions within the host matrix.

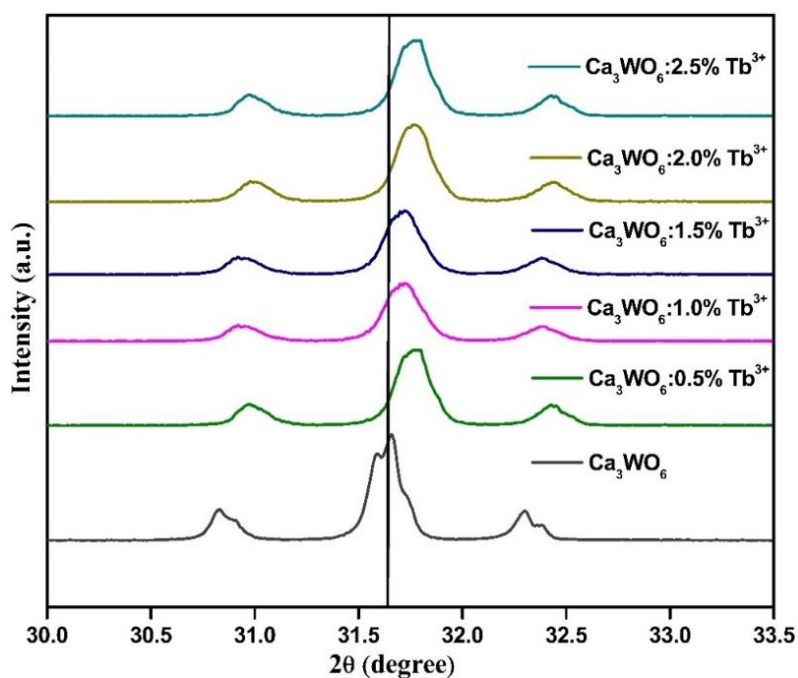


Figure 5.3. Magnified diffraction patterns of undoped and Tb^{3+} doped Ca_3WO_6 phosphors.

Moreover, when we closely examine the diffraction pattern, it is observed that the diffraction peak in the XRD patterns of the doped samples has shifted to a higher diffraction angle, as shown in Figure 5.3. This phenomenon of shifting in the diffraction angle can be explained by Vegard's law [25]. The shift of the diffraction peak towards a higher diffraction angle is due to the fact that the smaller radius cation Tb^{3+} takes the place of the larger radius cation Ca^{2+} within the structure. The calculation of D_r and observable shifting in diffraction

peak provides enough evidence, that the dopant Tb^{3+} is situated at the place of Ca^{2+} within parent crystal structure.

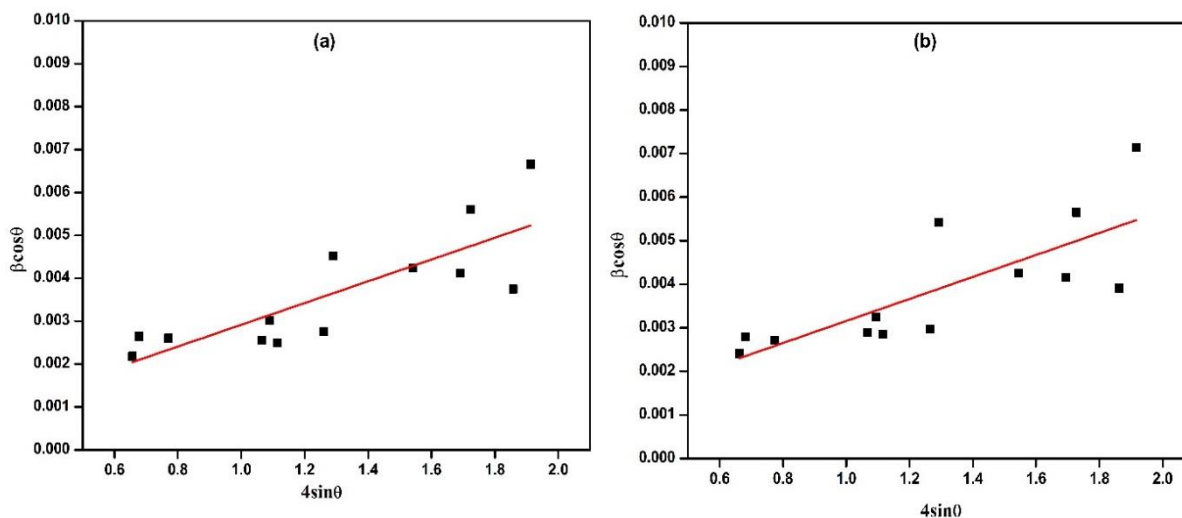


Figure 5.4. W-H plots of Ca_3WO_6 (a) and $Ca_3WO_6:0.5\% Tb^{3+}$ (b).

From the acquired XRD data, the average crystallite size of all the phosphors under study was calculated by using two different approaches, the Debye-Scherrer formula, and the Williamson-Hall (W-H) plot approach. Figure 5.4 illustrates the W-H plots for both the undoped (a) and 0.5 mol% Tb^{3+} doped (b) Ca_3WO_6 phosphors. As we increase the doping concentrations, we observe a reduction in the average crystallite size of the phosphors. Variations in the ionic radii between Ca^{2+} and the doping ions can lead to lattice distortion, which influences the crystallite size of the resulting crystal structure. The average crystallite sizes obtained from two different methods are presented in Table 5.2. Among both utilized methods of crystallite size calculation, the W-H plot method of crystallite size calculation was found more accurate.

Sample	Crystallite size (nm)	
	Debye-Scherrer	W-H Plot
Ca_3WO_6	48.54	54.58
$Ca_3WO_6: 0.5\% Tb^{3+}$	41.78	54.08
$Ca_3WO_6: 1.0\% Tb^{3+}$	46.34	53.32
$Ca_3WO_6: 1.5\% Tb^{3+}$	43.62	51.73
$Ca_3WO_6: 2.0\% Tb^{3+}$	45.15	51.52
$Ca_3WO_6: 2.5\% Tb^{3+}$	47.26	52.12

Table 5.2. Estimated crystallite size of the studied samples using two different methods.

5.3.2 SEM Studies

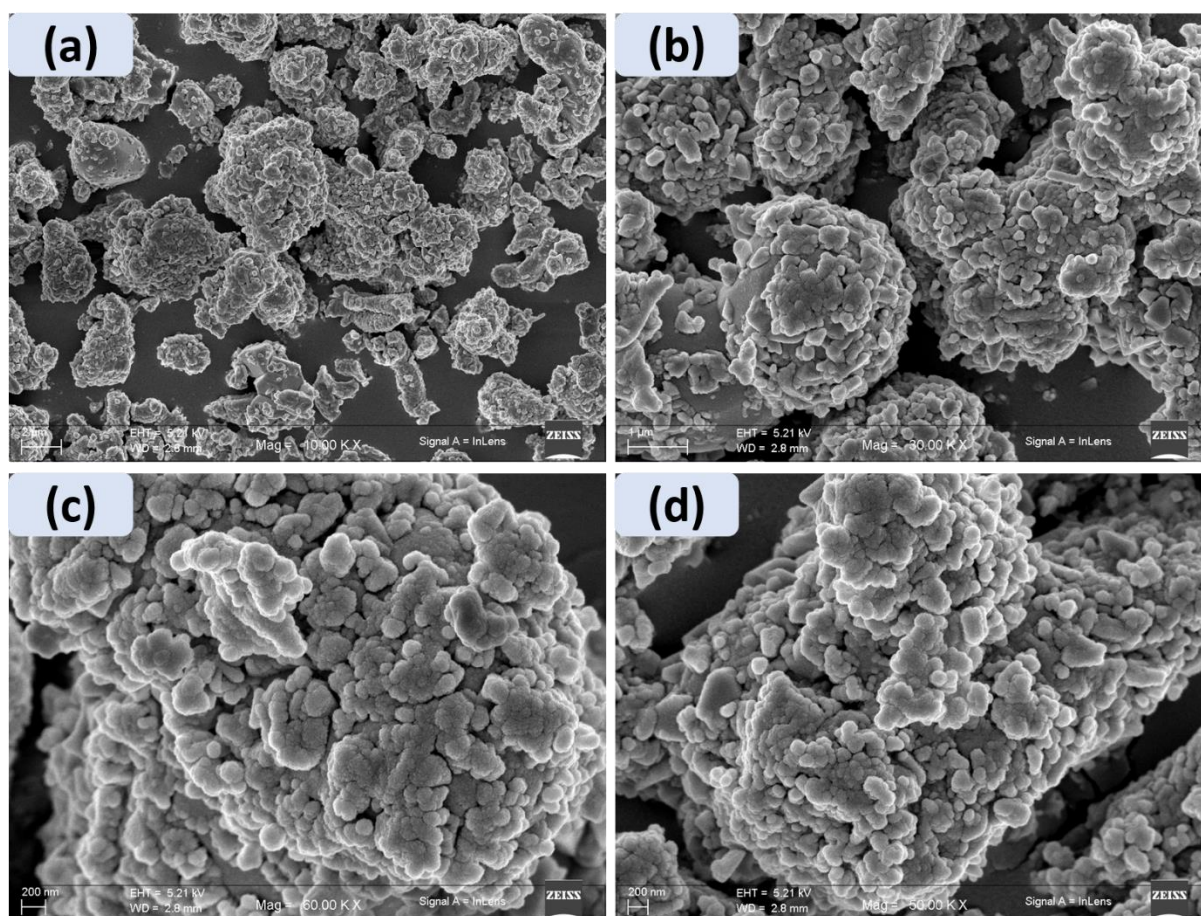


Figure 5.5. (a-d) SEM micrographs of 1 mol% Tb^{3+} doped Ca_3WO_6 phosphor.

Figure 5.5 (a-d) depicts the FESEM micrographs of 1 mol% Tb^{3+} phosphor under study. The different scanning resolutions are used to study the surface of the phosphor, mainly 200 nm, 1 μm , and 2 μm . The FESEM results displayed a high degree of agglomeration with non-uniform shapes and size of the phosphor particle. From the Figure 5.5. (d) it is observed that the majority of the particles are distributed within the range of a few nanometres to a micrometre.

5.3.3 EDAX Studies

EDAX is a technique used in materials science to govern the elemental composition of synthesized materials. Herein, 1 mol% Tb^{3+} doped Ca_3WO_6 phosphor was undergone through EDAX and results are depicted in Figure 5.6. From the figure, the sample displays different peaks consistent with each essential elements Ca, W, O, and dopant Tb. The observation from EDAX analysis confirms the successful doping of Tb^{3+} within the host matrix.

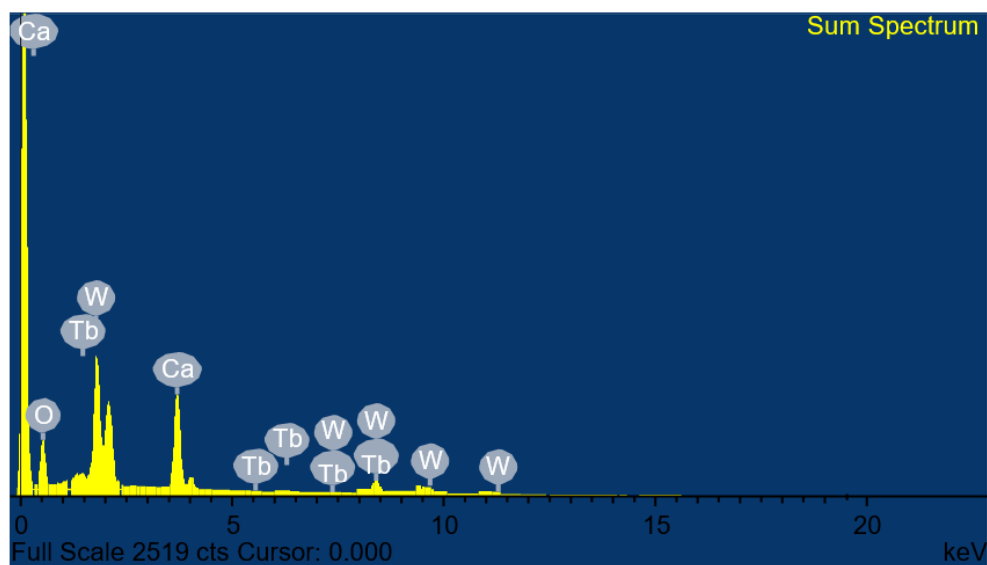


Figure 5.6. EDAX spectrum of 1 mol% Tb^{3+} doped Ca_3WO_6 phosphor.

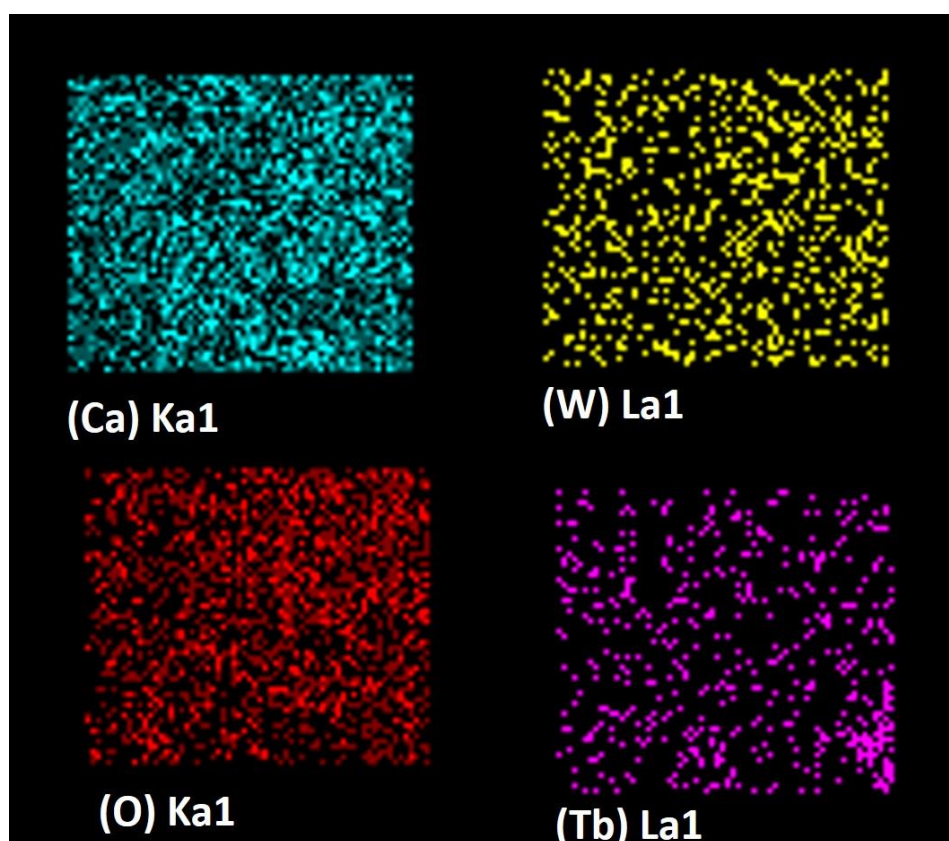


Figure 5.7. Elemental mapping of the 1 mol% Tb^{3+} doped Ca_3WO_6 phosphor.

Moreover, the elemental distribution mapping is depicted in Figure 5.7. From the figure, the presence of the constituent elements, namely Ca, W, O, and Tb, is clearly visible in separate color-coded images. These elemental mapping expose a regular spreading of all constituent elements within the material. Not only the host matrix elements, but also a slightly added Eu^{3+} dopant ions also look regularly dispersed throughout the material, which is due to the proper grinding of the raw materials before and after calcination.

5.3.4 FTIR Studies

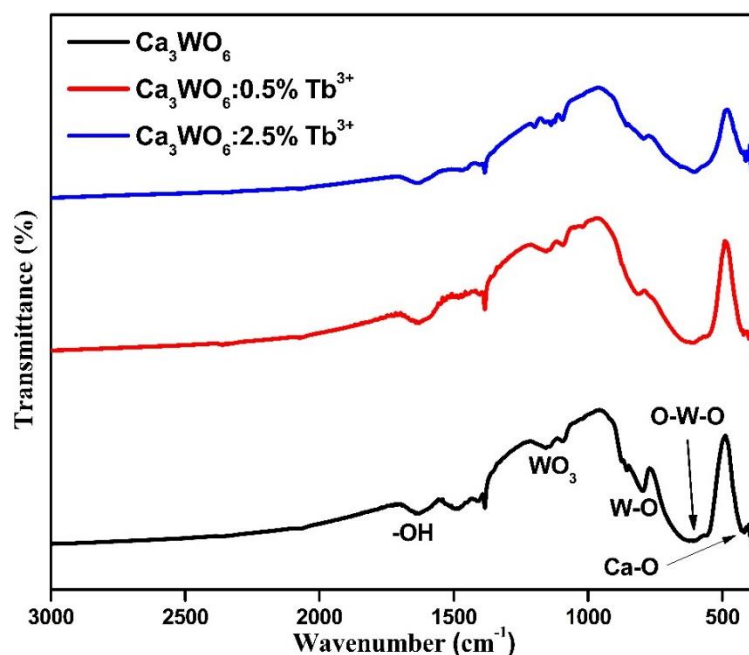


Figure 5.8. FTIR spectra of $\text{Ca}_3\text{WO}_6:\text{Tb}^{3+}$ double perovskite phosphors.

The investigation of functional groups present in the studied phosphors was conducted using FTIR spectroscopy. Figure 5.8 depicts the FTIR spectra of undoped, 0.5 mol% doped, and 2.5 mol% Tb^{3+} doped Ca_3WO_6 phosphors. The FTIR spectra were recorded using the KBr (Potassium bromide) pellet technique. The FTIR spectra of the mentioned phosphors exhibited prominent similarity. Within these spectra, distinct absorption bands corresponding to different bonds of calcium-oxide and tungstate were identified. The broad IR absorption band in the wavenumber range of $530\text{--}730\text{ cm}^{-1}$ can be attributed to the stretching vibration of O-W-O [26]. The absorption band with a sharp spike nature centered at 796 cm^{-1} arises from the crystallized W-O network present in the phosphor system [27]. Another shoulder IR band appearing at around 1150 cm^{-1} corresponds to the WO_3 functional group [28,29]. Furthermore, the bending vibration associated with absorbed moisture during measurement is detected at 1629 cm^{-1} , arisen may due to $\text{KBr}(\text{H-OH})_n$ carriers. However, an absorption band peaking towards the lower wavenumber side at 428 cm^{-1} indicates the presence of Ca-O lattice vibration [30]. Despite the prominent similarity in the FTIR spectra, the bonding between neighbouring atoms remains consistent upon Tb^{3+} doping.

5.3.5 Photoluminescence Studies

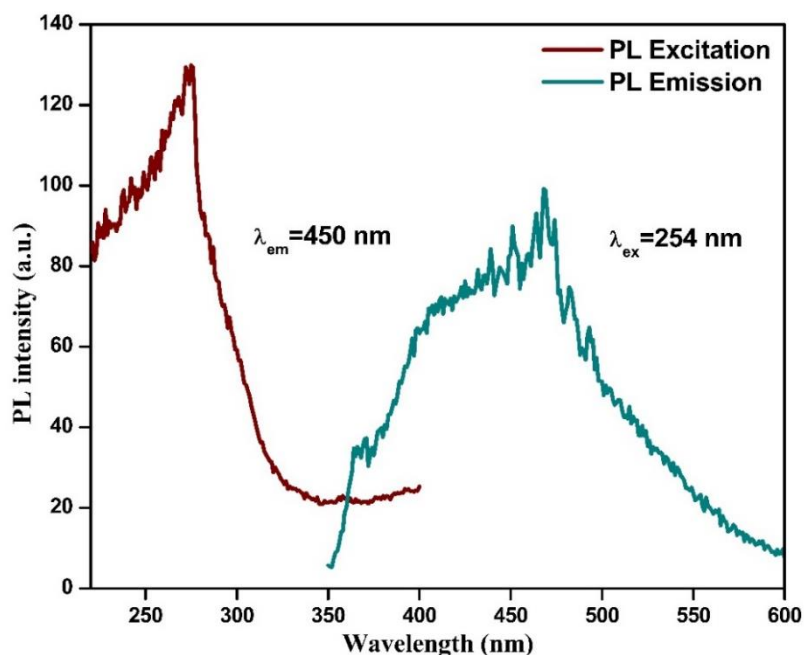


Figure 5.9. Photoluminescence excitation and emission spectra of pure Ca_3WO_6 .

Figure 5.9 depicts the PL excitation and emission spectra of base material Ca_3WO_6 . The PL excitation is monitored with 450 nm emission wavelength. The PL emission is monitored with an excitation wavelength of 254 nm. From the emission spectrum, it is found that the PL intensity is highest at 450 nm and a hump at 420 nm. This emission from the host lattice is an interesting feature of selecting it for luminescence investigation.

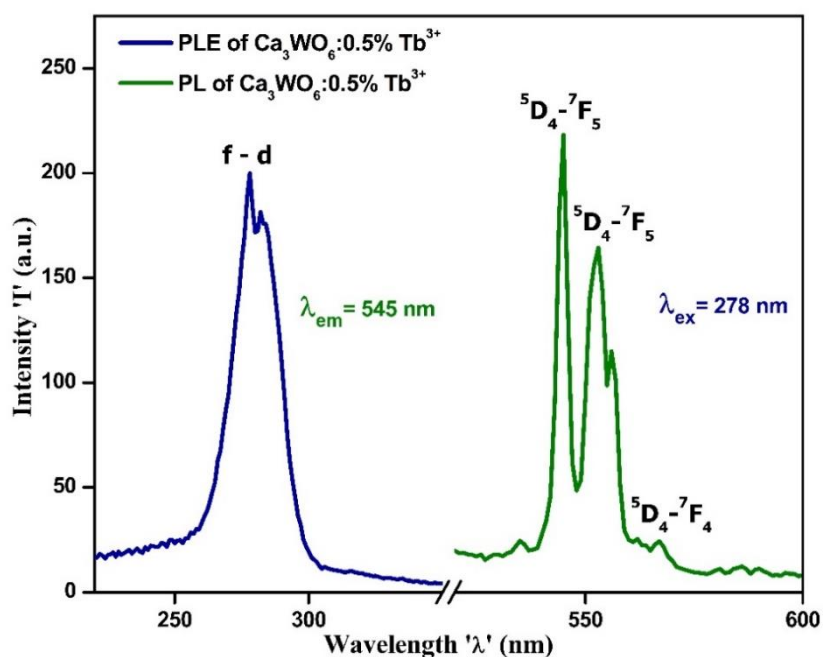


Figure 5.10. PL excitation and PL emission spectra of $\text{Ca}_3\text{WO}_6: 0.5\% \text{Tb}^{3+}$ phosphor.

To get green emission, terbium is the first choice to be employed as an activator in the host matrices due to its predominant transition occurring between 5D_4 - 7F_5 levels. The doping of terbium not only gives the green luminescence, but also shows fine tunability within green spectral region upon varying doping concentrations. Nemours study on Tb^{3+} activated phosphors are reported previously, the examples include, $Ca_2GeO_4:Tb^{3+}$ [31], $CsAlSi_2O_6:Tb^{3+}$ [32], and $CePO_4:Tb$ [33].

Figure 5.10 illustrates the photoluminescence excitation (PLE) and emission spectra of $Ca_3WO_6:0.5\% Tb^{3+}$ phosphor recorded at room-temperature (25 °C). The excitation spectrum of $Ca_3WO_6:0.5\% Tb^{3+}$ was recorded within the wavelength range of 220-400 nm, while the monitoring wavelength of 545 nm was used. The excitation spectrum of the mentioned phosphor consists of a broad band with an intense spike centered at 278 nm. This broad excitation peak in the excitation spectrum arises from the allowed $4f^8-4f^7 5d^1$ (f-d) transition of Tb^{3+} [33]. The nature of excitation indicates that the phosphors doped with various Tb^{3+} concentrations can be effectively excited by UV light of 278 nm. The emission spectrum of $Ca_3WO_6:0.5\% Tb^{3+}$ phosphor was recorded using an excitation wavelength of 278 nm, within the wavelength range of 400-600 nm. Electronic transitions occurring within the $4f^8$ state of terbium result in visible green emission at 545 nm. Herein, the emission resulting from the 5D_4 - 7F_J ($J=3-6$) transitions of Tb^{3+} collectively made the green spectral emission upon optical excitation [33,34]. Among these transitions, intensity due to the 5D_4 - 7F_5 (545 nm) transition of Tb^{3+} in emission spectra is the dominant one. The PL emission spectrum of $Ca_3WO_6:0.5\% Tb^{3+}$ phosphor exhibited three distinct emission peaks situated at 545 nm, 553 nm, and 567 nm. These three major emission peaks at 545 nm, 553 nm, and 567 nm correspond to the 5D_4 - 7F_5 , 5D_4 - 7F_5 , and 5D_4 - 7F_4 transitions of Tb^{3+} , respectively [35].

The intensity of PL emission is significantly influenced by the concentrations of activator ions. If the dopant concentration exceeds a certain threshold, the PL intensity gets quenched. This reduction in intensity is attributed to the decreased distance between consecutive dopant ions as the doping ion concentration increases. The reduced distance between neighbouring doping atoms causes non-radiative energy transfer, leading to intensity quenching [36]. Figure 5.11 illustrates the PL emission spectra of $Ca_3WO_6:Tb^{3+}$ phosphors, in which the concentration of Tb^{3+} varies from 0.5 mol% to 2.5 mol% in intervals of 0.5 mol%. It is evident from the spectra that the PL intensity initially increases as the doping concentration rises from 0.5 mol% to 1 mol%. Doping of 1.5 mol% Tb^{3+} resulted in intensity quenching. This phenomenon remained true for the doping of 2 mol% and 2.5 mol% of Tb^{3+} doping.

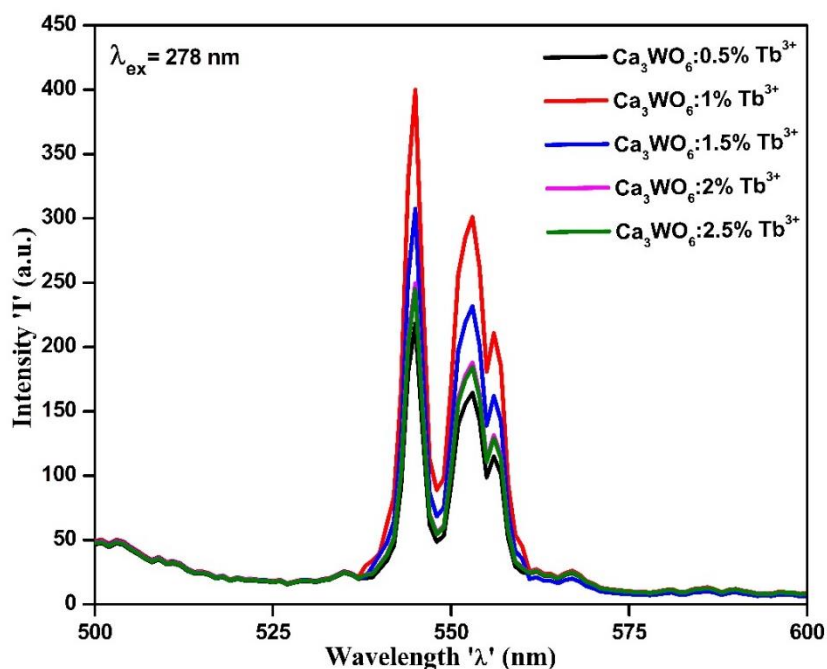


Figure 5.11. PL emission spectra of Ca_3WO_6 : $x\%$ Tb^{3+} ($x=0.5, 1, 1.5, 2, 2.5$) phosphors.

The relation between the PL intensity and Tb^{3+} concentration is depicted in Figure 5.12. The maximum PL intensity is achieved when the phosphor is doped with 1 mol% of Tb^{3+} . However, further increments in the doping concentration result in intensity quenching. The doping of 1.5 mol% of Tb^{3+} gives rise to intensity quenching. As mentioned earlier, the non-radiative energy transfer among Tb^{3+} activators are the cause of intensity quenching, and the phenomenon of multipolar interaction or exchange interaction is the responsible aspect [37].

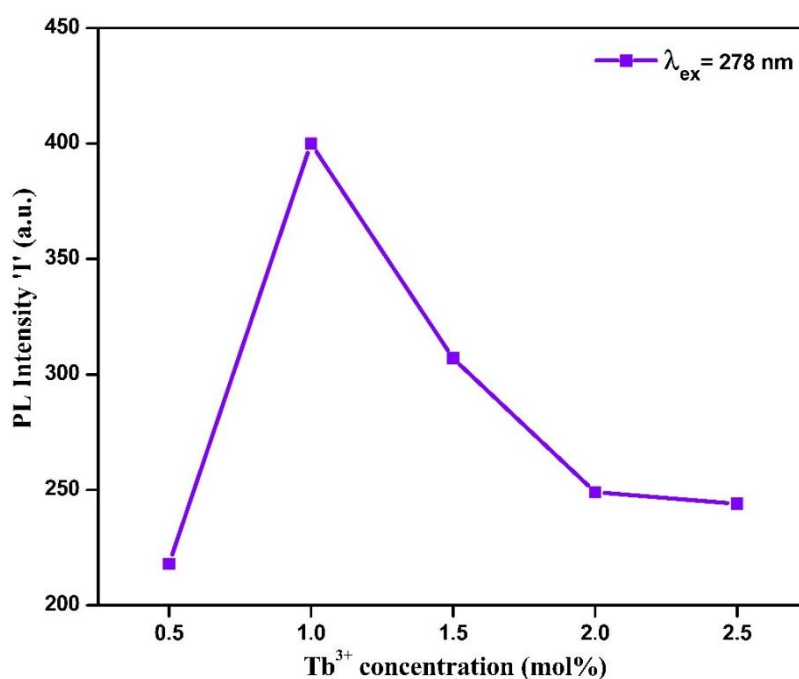


Figure 5.12. Plot of PL intensity as a function doping concentration.

To find out the specific mechanism of concentration quenching, Blasse introduced the concept of critical distance (R_c). Findings of critical distance can be applied in order to confirm the mechanism of concentration quenching, whether it was mediated by multipolar interaction or exchange interaction. By using formula 3.6, the R_c is computed. In the case of terbium doped Ca_3WO_6 phosphor, the R_c value was determined to be 18.28 \AA ($>5 \text{ \AA}$). This is strongly indicating that the concentration quenching was observed in phosphors having more than 1.5 mol% Tb^{3+} doping is only due to electric multipole-multipole interactions [38].

The investigation of phosphor performance of efficient luminescence involved the examination of CIE color coordinates and substantial color purity. The CIE chromaticity coordinates for $\text{Ca}_3\text{WO}_6:\text{Tb}^{3+}$ phosphors were determined using photoluminescence (PL) data. Figure 5.13 depicts the chromaticity coordinates for a Ca_3WO_6 phosphor doped with 1 mol% Tb^{3+} . When the phosphor was excited with a 278 nm wavelength, the color coordinates were obtained to $x=0.299$ and $y=0.675$. The calculated CIE color coordinates from the acquired PL data were found nearly equal to the standard green color CIE points [39,40]. As shown in Figure 5.13, the depiction of computed CIE point fall within the green spectral region of CIE diagram.

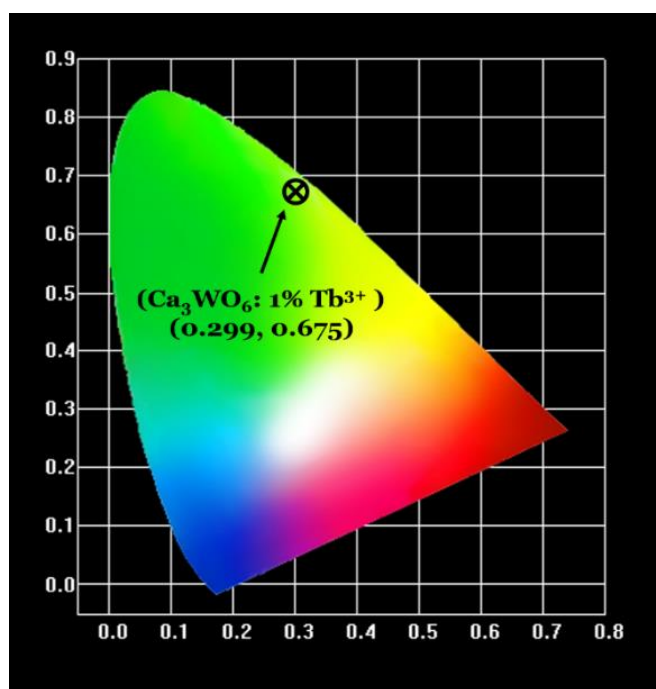


Figure 5.13. CIE diagram of 1 mol% Tb^{3+} doped Ca_3WO_6 phosphor.

Moreover, the color purity, an additional factor that inspects the phosphor performance was also calculated using formula 3.11. The CIE color coordinates and the color purity of all the phosphors under study are summarized in Table 5.3.

Sample	Chromaticity coordinates		Color purity (%)
	X	Y	
	Ca ₃ WO ₆ : 0.5% Tb ³⁺	0.298	
Ca ₃ WO ₆ : 1% Tb ³⁺	0.299	0.675	87.52
Ca ₃ WO ₆ : 1.5% Tb ³⁺	0.292	0.677	88.07
Ca ₃ WO ₆ : 2% Tb ³⁺	0.298	0.669	86.06
Ca ₃ WO ₆ : 2.5% Tb ³⁺	0.298	0.669	86.06

Table 5.3. Summary of CIE color coordinates and color purity of Ca₃WO₆:Tb³⁺ phosphors.

5.3.6 Thermoluminescence Studies

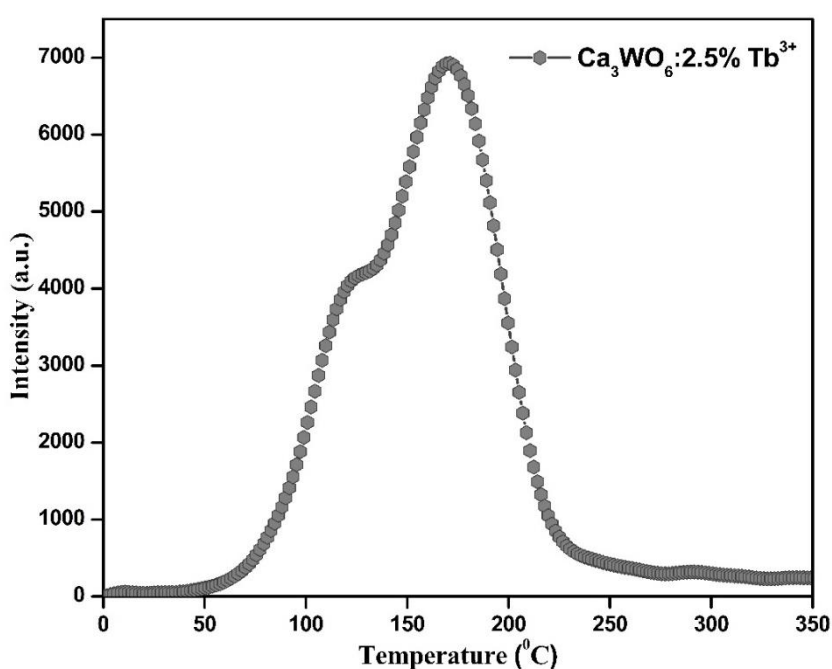


Figure 5.14. TL glow curve of Ca₃WO₆:2.5% Tb³⁺ phosphor irradiated with 50 Gy of beta rays.

First, the TL of Ca₃WO₆ double perovskite with 2.5 mol% of Tb³⁺, the phosphor having highest doping level, was recorded after irradiating with beta rays using a Sr-90 beta source. Figure 5.14 illustrates the acquired TL glow curve of Ca₃WO₆:2.5% Tb³⁺ phosphor after exposure of 50 Gy beta dose. The measurement was taken over a temperature range of 0 °C to 350 °C, with steady heating rate of 2°C/s. The Ca₃WO₆:2.5% Tb³⁺ phosphor exhibited an extraordinary TL glow curve with outstanding glow intensity upon beta irradiation. The TL glow curve typically comprises an intense glow peak centered at around 171°C together with a hump towards lower temperature site at around 117 °C. This nature of TL glow curve suggests the formation of two trapping centres within the phosphor under beta irradiation [41,42]. It

should be mentioned that the beta rays have capability to penetrate the materials and create deeper trapping centres rather than surface defects. This phenomenon implies that the beta irradiation produces defects inside the crystal lattice. In the present phosphor system, the recombination of the trapped charge carriers at deeper trapping centre resulting in highly intense and sensitive glow curve under controlled heating.

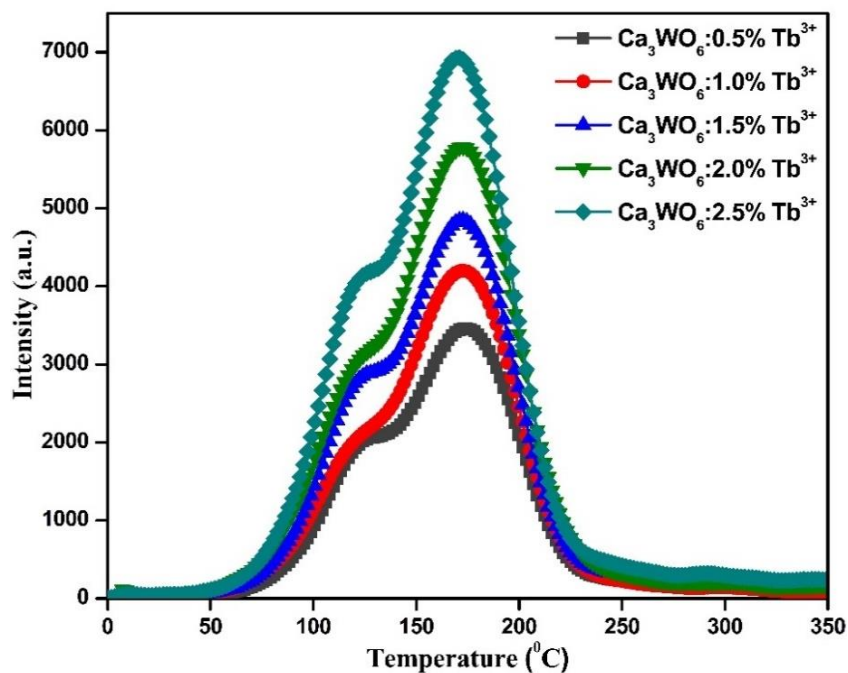


Figure 5.15. TL glow curves of $\text{Ca}_3\text{WO}_6:x\% \text{Tb}^{3+}$ ($x=0.5-2.5$) phosphors after 50 Gy of beta irradiation.

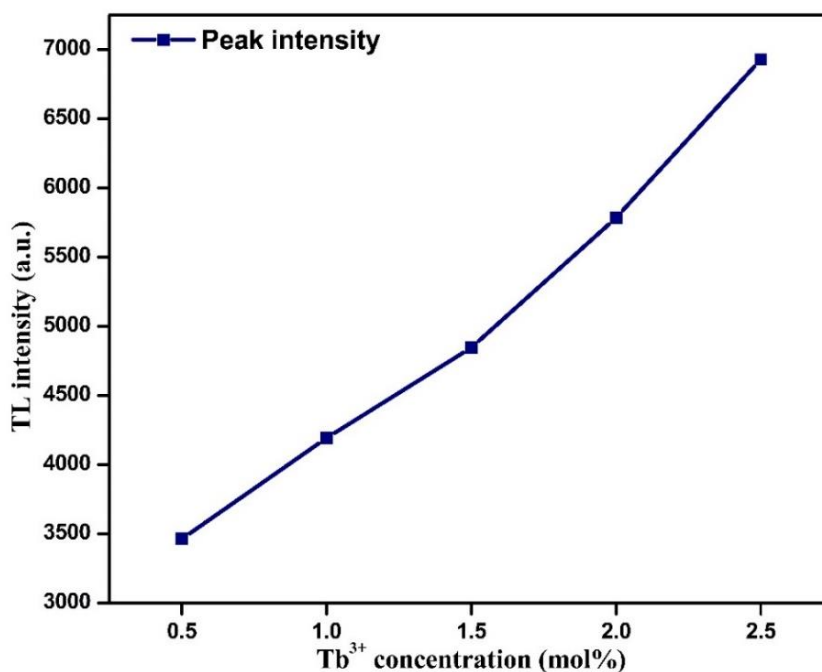


Figure 5.16. TL intensity response to different Tb^{3+} concentrations.

To investigate the impact of varying Tb^{3+} concentrations on the TL intensity, the glow curves of Ca_3WO_6 materials doped with diverse Tb^{3+} levels were recorded after 50 Gy dose of beta irradiation, and are illustrated in figure 5.15. The intensity of TL glow curves found significantly influenced by the dopant concentration. To understand the TL response toward Tb^{3+} concentration, the intensity of TL was plotted against Tb^{3+} concentration, shown in Figure 5.16. As Tb^{3+} concentration increases, the intensity of the most intense TL peak is progressively enhanced, while the shape of the glow curve remains unchanged. When the phosphor is doped with a concentration of 2.5 mol% of Tb^{3+} , highest TL intensity is observed among all studied samples. Obtained results suggest that the ordered increment in doping concentration of Tb^{3+} into the host matrix, leads to a substantial increase in trapping centres [43,44]. As the $Ca_3WO_6:2.5\ mol\% Tb^{3+}$ phosphor shows the highest TL intensity counts, the dose-response study and fading effect study were carried out on this sample only.

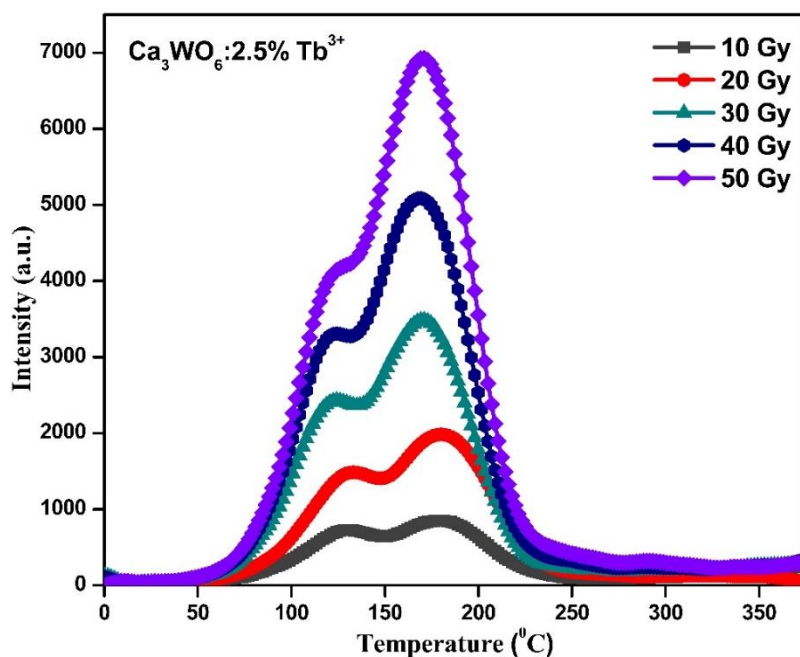


Figure 5.17. TL glow curves of $Ca_3WO_6:2.5\% Tb^{3+}$ phosphor at different doses of beta irradiation.

The TL dosimetry requirement is a linear growth response for any ionizing radiation. The same is studied for the $Ca_3WO_6:2.5\% Tb^{3+}$ phosphor under study. To understand the dose response in this TL study, the phosphors under investigation were exposed to a wide range of beta doses, primarily from 10 to 50 Gy. Figure 5.17 depicts the TL glow curves of the $Ca_3WO_6:2.5\% Tb^{3+}$ phosphor at specific beta doses. The intensity of the TL glow peak tends to rise with increasing ionizing radiation dose. This observation suggests that the number of trapping centres increased as the absorption of beta irradiation increased. As a result, the

intensity of TL looks enhanced. The absorption of ionizing radiation is directly reflected in TL intensity counts [45]. However, we did not detect any significant changes in the shape of the glow curve or the peak temperature.

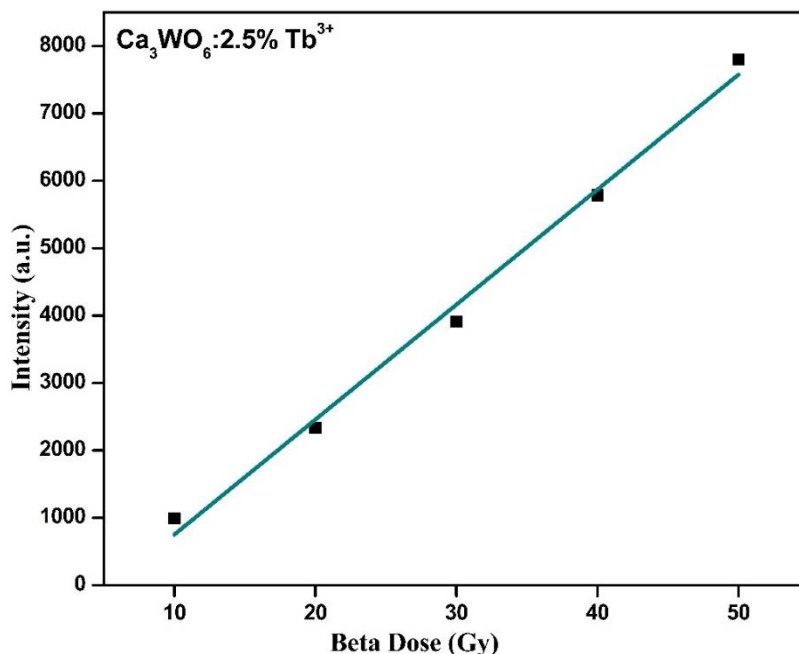


Figure 5.18. Dose response of $\text{Ca}_3\text{WO}_6:2.5\% \text{Tb}^{3+}$ phosphor towards beta rays.

In addition, a plot of TL intensity as a function of the beta dose was drawn in order to examine the linear dose-response, as shown in the Figure 5.18. The relationship between intensity and concerned beta dose illustrates excellent linearity, indicating a progressive increase in the generation of defect centres with increasing beta dose. The results from dose-response study propose that the studied phosphor can be considered as TL dosimetry phosphor.

To assess the long-term radiation dose storage capacity of the phosphor, it is essential to examine the phenomenon of intensity fading [46]. In the presence of sunlight, there is a solid possibility of recombination of the trapped charges which were created during ionizing radiation exposure. This recombination mainly occurs in the case of shallow traps. However, trapping centers generated by high-energy radiation tend to be deeper and exhibit long stability. A good TL dosimeter should exhibit negligible fading rates for absorbed dose [47].

To investigate the fading effect in the studied phosphor, an equally weighted $\text{Ca}_3\text{WO}_6:2.5\% \text{Tb}^{3+}$ phosphor powders were exposed to beta radiation at a dose of 50 Gy. Afterwards, these irradiated phosphors were stored in a dark environment under ambient conditions. The first TL measurement was taken direct after beta irradiation, and then in interval of five days, the measurements were taken for next 30 days. The TL glow curves recorded after mentioned time interval after beta irradiation, are presented in figure 5.19 (a). As shown in

figure, a very slight reduction in TL intensity was observed, in addition with minor shift of TL peak towards higher temperature. This shifting in the peak position may indicate that the defect created upon beta irradiation become more deeper with time, and stay sustained rather than recombine with hole.

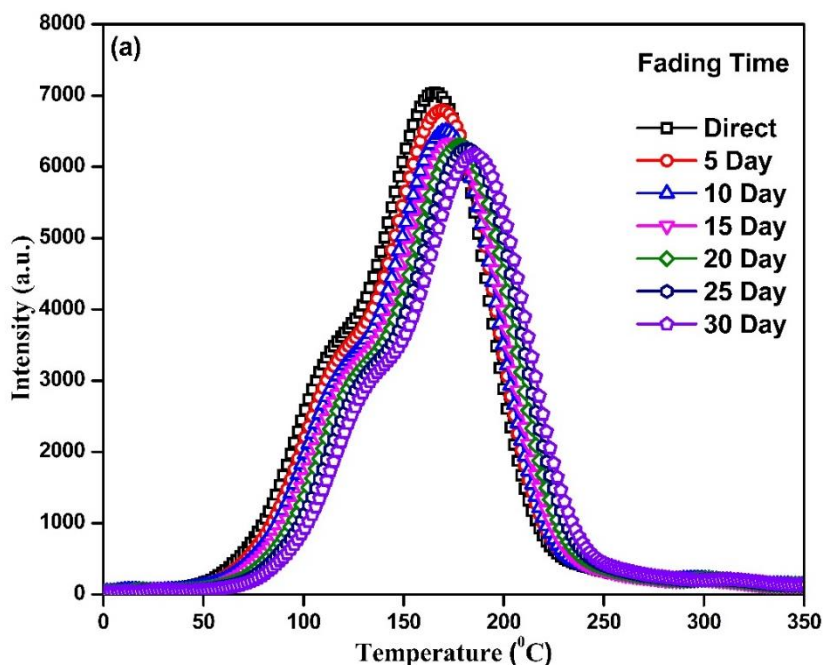


Figure 5.19. (a) TL glow curves of $\text{Ca}_3\text{WO}_6:2.5\% \text{Tb}^{3+}$ after 30 days of irradiation.

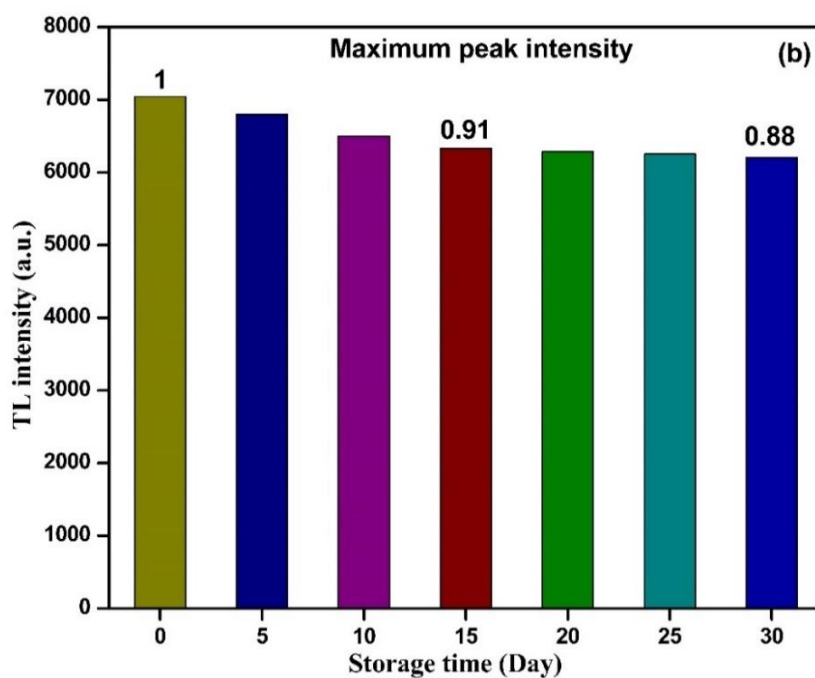


Figure 5.19. (b) Comparative TL intensities of $\text{Ca}_3\text{WO}_6:2.5\% \text{Tb}^{3+}$ after 30 days of irradiation.

Figure 5.19 (b) illustrates the comparative TL intensities of the investigated phosphor after 30 days of irradiation. Initially for first 15 days, an average fading in TL intensity of approximately 9% was observed when compared to the initial TL intensity count taken immediately after irradiation. Subsequently, over the passage of one month, a fading of around 12% was observed. This 12% of fading value demonstrates the favourable stability of the deeper traps inside studied phosphor. The minimal fading observed during this considered period suggests that the $\text{Ca}_3\text{WO}_6:2.5\% \text{Tb}^{3+}$ phosphor holds potential for applications in TLD for high doses of beta rays.

The trapping constants, namely trap depth (E_a), frequency factor (s), and order of kinetics associated with the obtained glow curve are needed to figure out for the understanding of the kinetic features. The examination of the glow curve discloses the information concerning trap parameters and followed order of kinetics by the investigational TL glow curves. Among varieties of calculation techniques, the Chen's peak shape method (PSM) and GCD method were applied to compute the trapping constants.

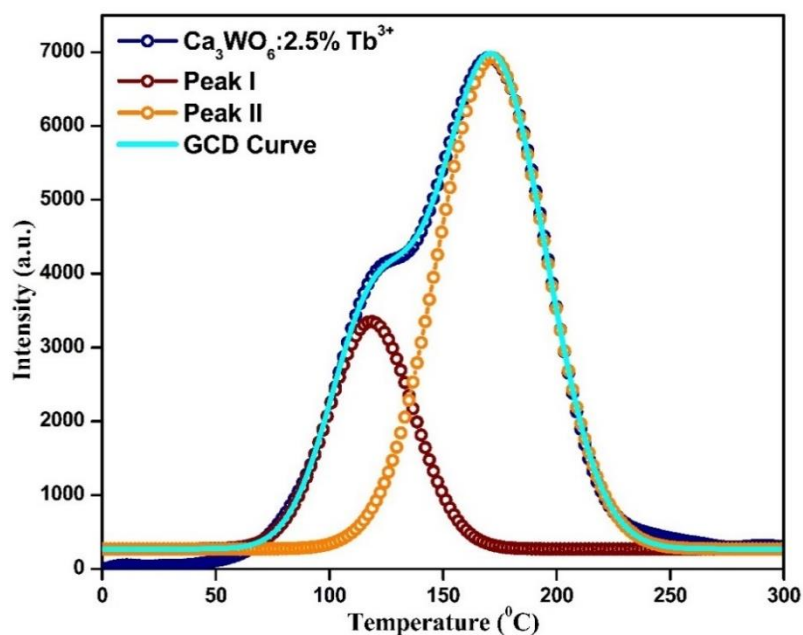


Figure 5.20. Deconvoluted TL glow curve of $\text{Ca}_3\text{WO}_6:2.5\% \text{Tb}^{3+}$ phosphor.

Initially, the PSM for trap parameter determination was applied. Subsequently, the obtained TL glow curve of $\text{Ca}_3\text{WO}_6:2.5\% \text{Tb}^{3+}$ phosphor was deconvoluted first. Figure 5.20 illustrates the deconvoluted TL glow curve of the $\text{Ca}_3\text{WO}_6:2.5\% \text{Tb}^{3+}$ phosphor which was recorded after the exposure of 50 Gy dose of beta radiation. This deconvoluted curve exhibited two distinct glow peaks located at temperatures of 119°C (referred to as P1) and 171°C (referred to as P2). The calculated geometrical factor specifies that both deconvoluted peaks identified above follow second-order kinetics [48]. Subsequently, the E_a was computed via a

general formulation of activation energy proposed by Chen, and was valid for any order of kinetics. The obtained trap depths E_{τ} , E_{δ} and E_{ω} were lied between 0.96-1.04 eV, 0.99-1.05 eV and 0.98-1.06 eV, respectively. All PSM computed kinetic parameters were listed in Table 5.4.

Sample		T_{\max} (K)	μg	Activation Energy		
				E_{τ} (eV)	E_{δ} (eV)	E_{ω} (eV)
Ca ₃ WO ₆ : 0.5 mol% Tb ³⁺	Peak I	395	0.51	0.96±0.04	0.99±0.05	0.98±0.02
	Peak II	447	0.52	1.02±0.04	1.01±0.03	1.02±0.02
Ca ₃ WO ₆ : 1.0 mol% Tb ³⁺	Peak I	392	0.51	0.93±0.04	0.95±0.05	0.96±0.02
	Peak II	446	0.52	1.01±0.04	1.03±0.03	1.02±0.02
Ca ₃ WO ₆ : 1.5 mol% Tb ³⁺	Peak I	397	0.51	1.03±0.04	1.05±0.05	1.04±0.02
	Peak II	447	0.52	1.04±0.04	1.05±0.04	1.06±0.02
Ca ₃ WO ₆ : 2.0 mol% Tb ³⁺	Peak I	392	0.51	0.94±0.04	0.98±0.05	0.99±0.02
	Peak II	447	0.52	1.01±0.04	1.05±0.03	1.04±0.02
Ca ₃ WO ₆ : 2.5 mol% Tb ³⁺	Peak I	392	0.51	1.00±0.04	1.03±0.05	1.02±0.02
	Peak II	444	0.52	1.02±0.04	1.04±0.04	1.04±0.02

Table 5.4. Summary of trapping parameters calculated using Chen’s peak shape method.

Moreover, with the deconvoluted spectrum, the trapping constants were also computed using Kitis et al. equation for second-order kinetic. As stated in PSM, the second-order kinetics of both identified peaks were additionally confirmed by GCD. Kitis et al. formula for second-order kinetics was taken into the account and calculation of E_a was accomplished. The calculated trap depth via GCD method ranges between 0.87 eV and 1.00 eV, which is closely identical to the trap depths obtained via PSM. Trapping constants calculated with GCD technique are presented in Table 5.5.

Sample		T_{\max} (K)	Activation Energy ‘ E_a ’ (eV)	Order of Kinetics ‘ b ’	Frequency Factor ‘ s ’ (s ⁻¹)
	Peak II	447	0.96±0.12	2.00	2.51 × 10 ⁹
Ca ₃ WO ₆ : 1.0 mol% Tb ³⁺	Peak I	395	0.90±0.02	1.90	2.31 × 10 ⁹
	Peak II	446	0.94±0.11	2.00	1.45 × 10 ⁹
Ca ₃ WO ₆ : 1.5 mol% Tb ³⁺	Peak I	393	0.88±0.03	1.90	2.56 × 10 ⁹
	Peak II	446	0.97±0.11	2.00	4.23 × 10 ⁹
Ca ₃ WO ₆ : 2.0 mol% Tb ³⁺	Peak I	394	0.89±0.02	1.90	3.65 × 10 ⁹
	Peak II	446	1.00±0.11	2.00	7.01 × 10 ⁹
Ca ₃ WO ₆ : 2.5 mol% Tb ³⁺	Peak I	392	0.87±0.03	1.90	1.01 × 10 ⁹
	Peak II	444	1.00±0.10	1.90	1.76 × 10 ⁹

Table 5.5. Summary of TL kinetic parameters calculated by GCD method.

Part-II

Luminescence Studies of $\text{Ca}_3\text{WO}_6:\text{Ho}^{3+}$

The following section describes the luminescence studies of synthesized phosphor namely $\text{Ca}_3\text{WO}_6:\text{Ho}^{3+}$, the obtained results and characterizations.

5.4 Results and Discussion

5.4.1 XRD Studies

A study on refinement of the crystal structure of undoped Ca_3WO_6 was already discussed, as presented in Part-I of this chapter. Figure 5.21 demonstrates the X-ray diffraction (XRD) patterns of both pure Ca_3WO_6 and Ho^{3+} activated Ca_3WO_6 phosphors. A minor doping of Ho^{3+} not make any observable impact on the parent crystal structure, as all the recorded diffraction pattern looks nearly identical. Similar XRD patterns of all the tungstate phosphors represent that they all are crystalline to a pure monoclinic crystalline structure with P 21/c space group [20,21].

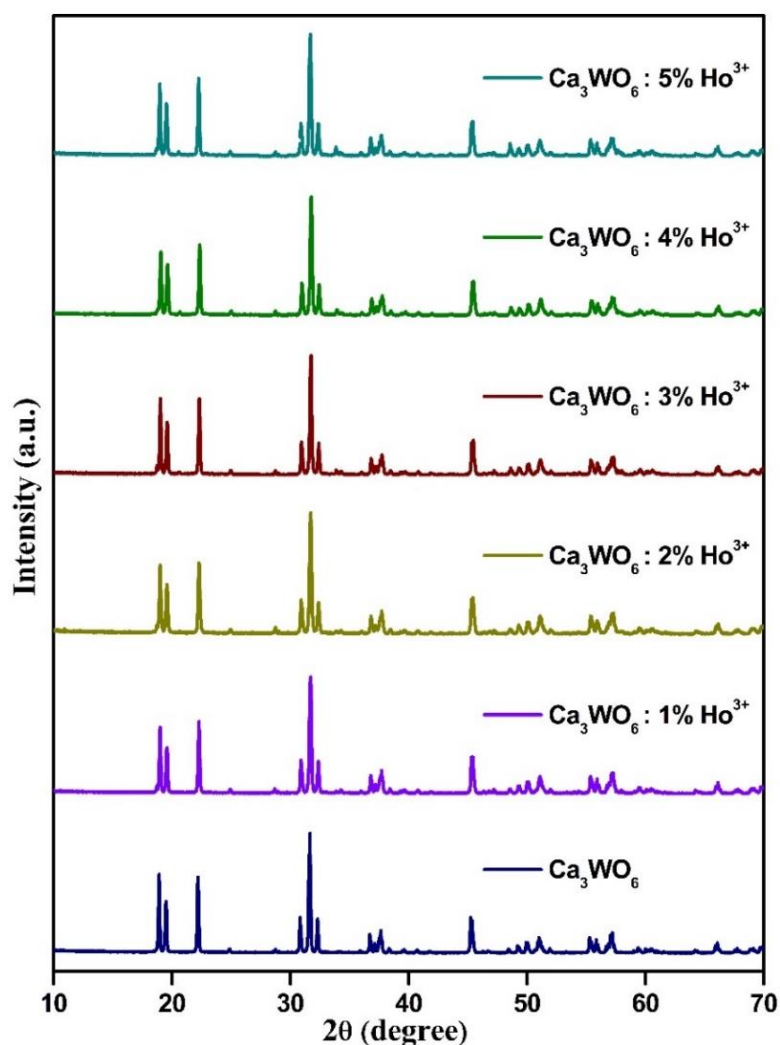


Figure 5.21. XRD patterns of Ca_3WO_6 : x mol% Ho^{3+} (x= 0-5) phosphors.

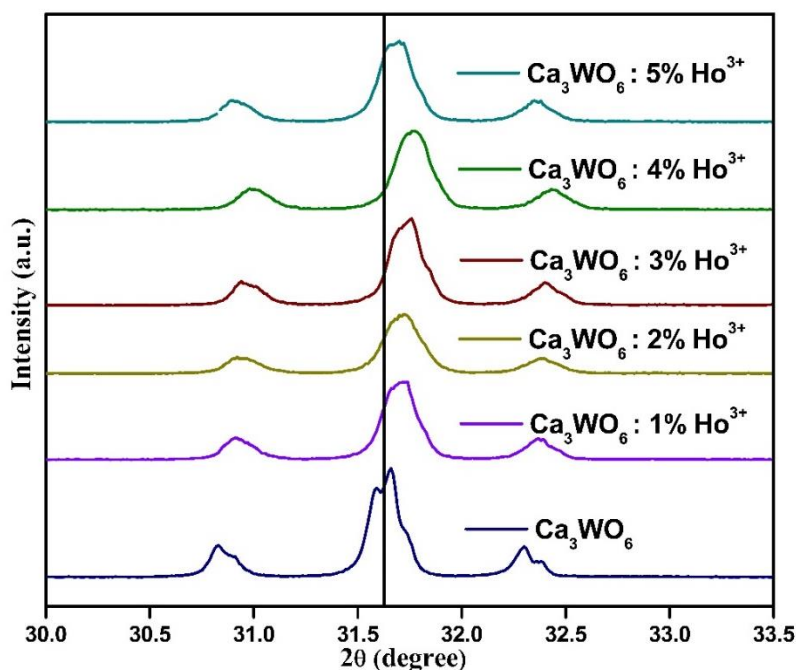


Figure 5.22. Magnified diffraction patterns of undoped and Ho^{3+} doped Ca_3WO_6 phosphors.

From Figure 5.21, it is observed that the diffraction patterns of both pure and Ho^{3+} doped phosphors appeared closely identical. In this situation, to identify the Ho^{3+} doping, the XRD pattern was magnified. Upon XRD magnification, a noticeable change in the XRD pattern was observed. When we magnified the diffraction patterns, an observable shift in the position of the most intense diffraction peak of the doped samples was detected, as depicted in Figure 5.22. This shift in the diffraction peak's position can be explained through Vegard's law [49]. It is observed that the diffraction peak located at 31.66° in the XRD patterns of the doped samples has been shifted towards higher diffraction angle. This is due to the fact that the smaller radius cation Ho^{3+} takes the place of the larger radius cation Ca^{2+} within the structure. In order to maintain $n\lambda$ constant in Bragg's formula, the diffraction angle should be move forward when a cation with a smaller radius replaces a cation with a larger radius. In addition, the calculation of D_r (acceptable percentage difference), the concept of ionic radii of the substituted and substituting ions, provides additional evidence that the dopant Ho^{3+} is situated at the place of Ca^{2+} within the parent crystal structure. The computed value of D_r is found to be 9.9 %, which further suggests the introduction of Ho^{3+} at the place of Ca^{2+} within the host lattice.

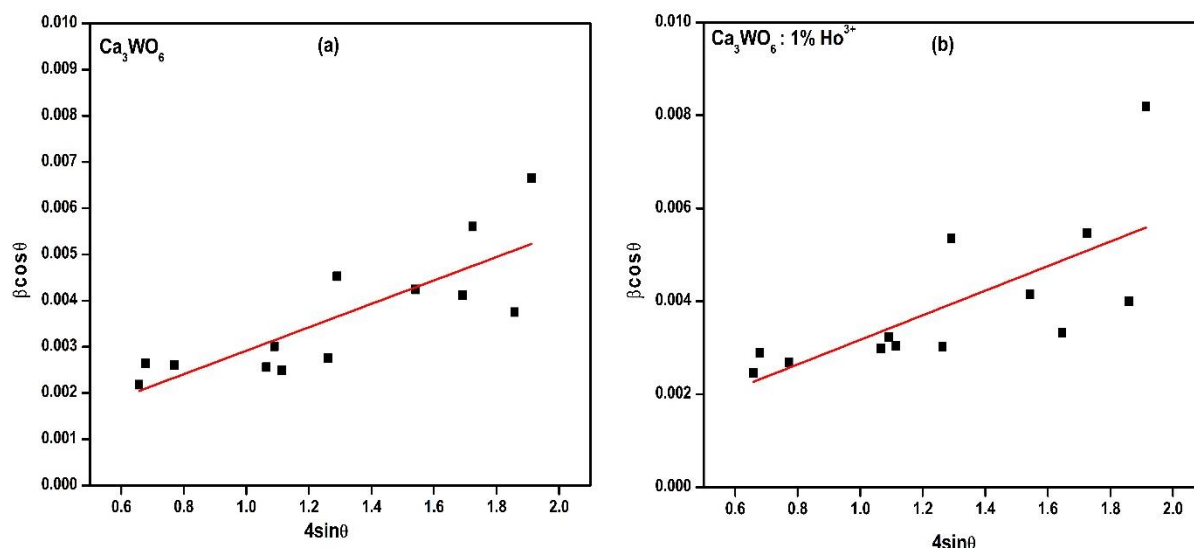


Figure 5.23. W-H plots of Ca_3WO_6 (a) and $\text{Ca}_3\text{WO}_6:1\% \text{Ho}^{3+}$ (b).

In addition, from the XRD data, the average crystallite size of the all-mentioned compositions was computed via W-H plot analysis and Debye-Scherrer formulation. Figure 5.23 depicts the W-H plots of the undoped (a) and 1 mol% Ho^{3+} doped Ca_3WO_6 phosphors. When crystallite size is calculated using Debye-Scherrer, nearly the same value of crystallite size was found. However, in the case of W-H plot analysis, the crystallite size seems to be slightly decreased upon increased doping concentration. Differences in the ionic radii of Ca^{2+} and dopant ions may result in lattice distortion, which reduces the crystallite size of the resultant crystal structure [50]. The average crystallite size calculated using two different approaches is tabulated in Table 5.6.

Sample	Crystallite size (nm)	
	Debye-Scherrer	W-H Plot
Ca_3WO_6	48.54	54.58
$\text{Ca}_3\text{WO}_6:1\% \text{Ho}^{3+}$	48.79	54.85
$\text{Ca}_3\text{WO}_6:2\% \text{Ho}^{3+}$	45.26	52.71
$\text{Ca}_3\text{WO}_6:3\% \text{Ho}^{3+}$	41.34	51.13
$\text{Ca}_3\text{WO}_6:4\% \text{Ho}^{3+}$	45.44	49.62
$\text{Ca}_3\text{WO}_6:5\% \text{Ho}^{3+}$	46.32	50.35

Table 5.6. Estimated crystallite size of the studied samples using two different methods.

5.4.2 SEM Studies

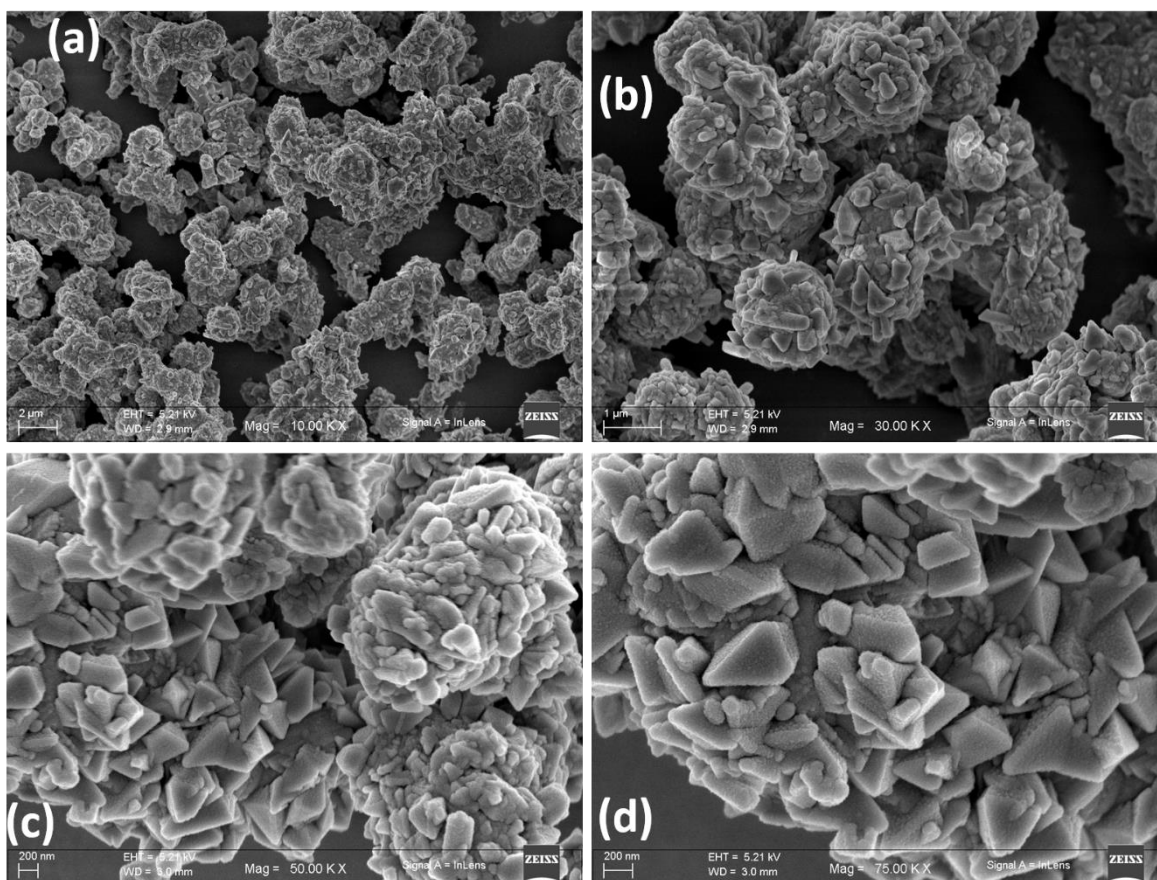


Figure 5.24. (a-d) SEM micrographs of 4 mol% Ho^{3+} doped Ca_3WO_6 phosphor.

The surface morphology and topography are studied using FESEM. Figure 5.24 (a-d) depicts the SEM micrographs of 4 mol% Ho^{3+} doped Ca_3WO_6 phosphor captured at different scanning resolutions, mainly 200 nm, 1 μm and 2 μm . From the figure it is observed that the micron-sized particles of the phosphor with irregular shapes and size were dispersed and appeared as a cluster. This porous morphology may observe due to the high-temperature calcination and the escaping gases during the calcination. From the Figure 5.24 (d), we concluded that the average size of the mixed phosphor particles ranges between a few nanometers ($\sim 200\text{-}500$ nm) to a ~ 2 μm .

From Figure 5.24 (c), the particle cluster seems bright, which is nothing but the cathodoluminescence that arises upon impinging high energy electron beam to study the surface morphology.

5.4.3 EDAX Studies

In addition, the chemical stoichiometry and purity of the material is ascertained via the EDAX analysis. Figure 5.25 depicts the EDAX spectra of the 4 mol% Ho^{3+} doped Ca_3WO_6

phosphor, wherein, all the constituent elements of the host matrix including Ca, W, O along with slightly added foreign element Ho is found.

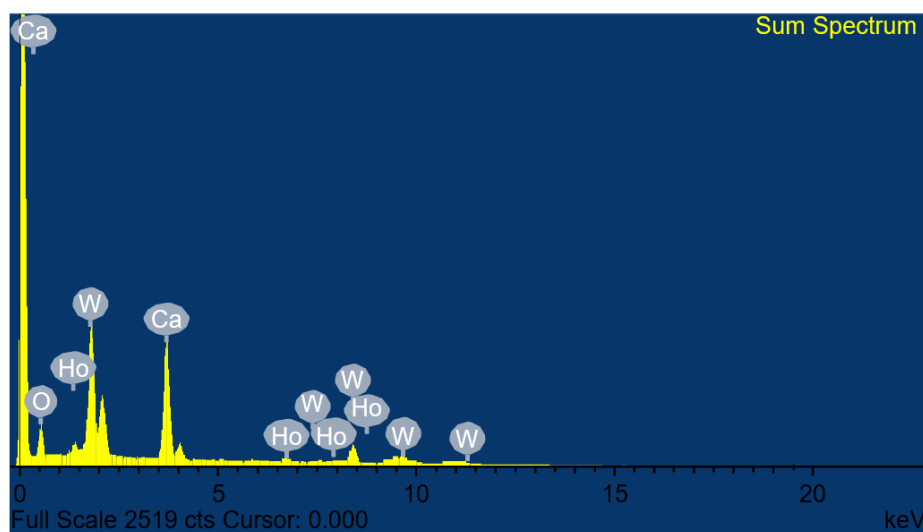


Figure 5.25. EDAX spectrum of 4 mol% Ho^{3+} doped Ca_3WO_6 phosphor.

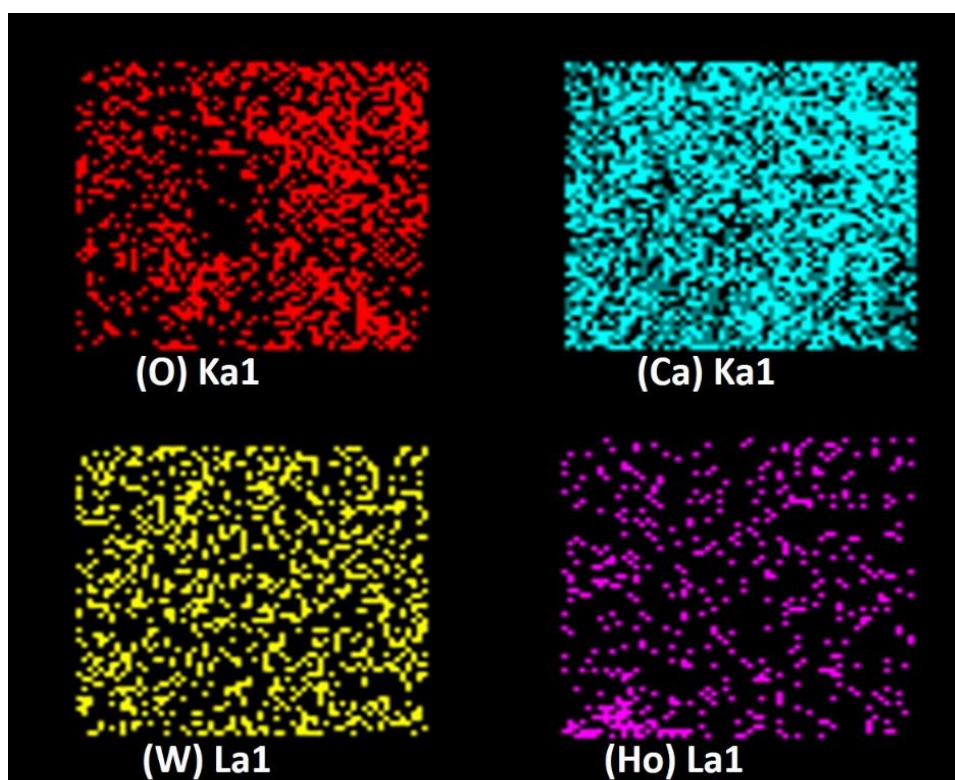


Figure 5.26. Elemental mapping of the 4 mol% Ho^{3+} doped Ca_3WO_6 phosphor.

Figure 5.26 depicts the elemental mapping of all the constituent elements. Each element of the prepared material is mapped separately in the colored images. From the mapping, it is observed, all the constituent elements including slightly doped impurity elements distributed evenly throughout the material. As a result, the observations from the EDAX analysis confirm the formation of $\text{Ca}_3\text{WO}_6:\text{Ho}^{3+}$ phosphor.

5.4.4 FTIR Studies

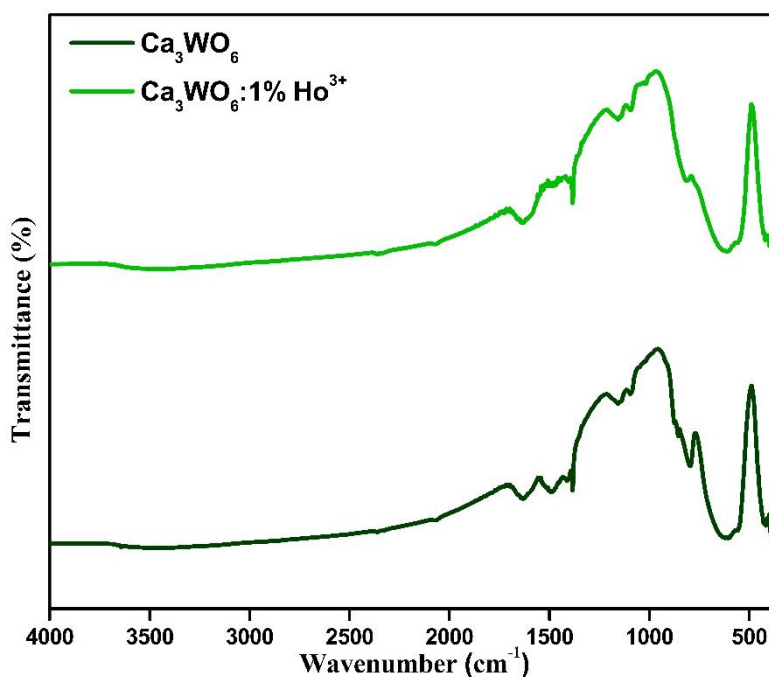


Figure 5.27. FTIR spectra of $\text{Ca}_3\text{WO}_6:\text{Ho}^{3+}$ double perovskite phosphors.

Figure 5.27 depicted the FTIR spectra of undoped, and 1 mol% Ho^{3+} doped Ca_3WO_6 phosphors. The KBr (Potassium bromide) pellet technique was employed to record the spectra. The FTIR spectra of undoped and Ho^{3+} doped phosphors look closely similar. As well as the IR spectra recorded for Ho^{3+} doped phosphor also look identical to the IR spectra of Tb^{3+} doped phosphor (Figure 5.8). As a result, all the observed vibrational modes are standard bonding vibrations, as defined in section 5.3.4.

5.4.5 Photoluminescence Studies

Except Tb^{3+} , holmium (Ho^{3+}) and erbium (Er^{3+}) are also be the choice to dope in order to produce green luminescence emission. Unlike some other luminescent activators, both Ho^{3+} and Er^{3+} can give up-conversion as well as down-conversion luminescence. Sometimes, only doping of Ho^{3+} or Er^{3+} also gives the green up-conversion luminescence, whereas, in some cases, sensitizers were needed to achieve up-conversion luminescence. The ytterbium (Yb^{3+}) comes with a unique feature as a sensitizer to have ability to absorb the lower energy radiation and transfer it to the activator. As a result, the energy transfer will take place between the activator and sensitizer, resulting in up-conversion luminescence. The up-conversion luminescence from a singly doped phosphor is achieved in the present sample.

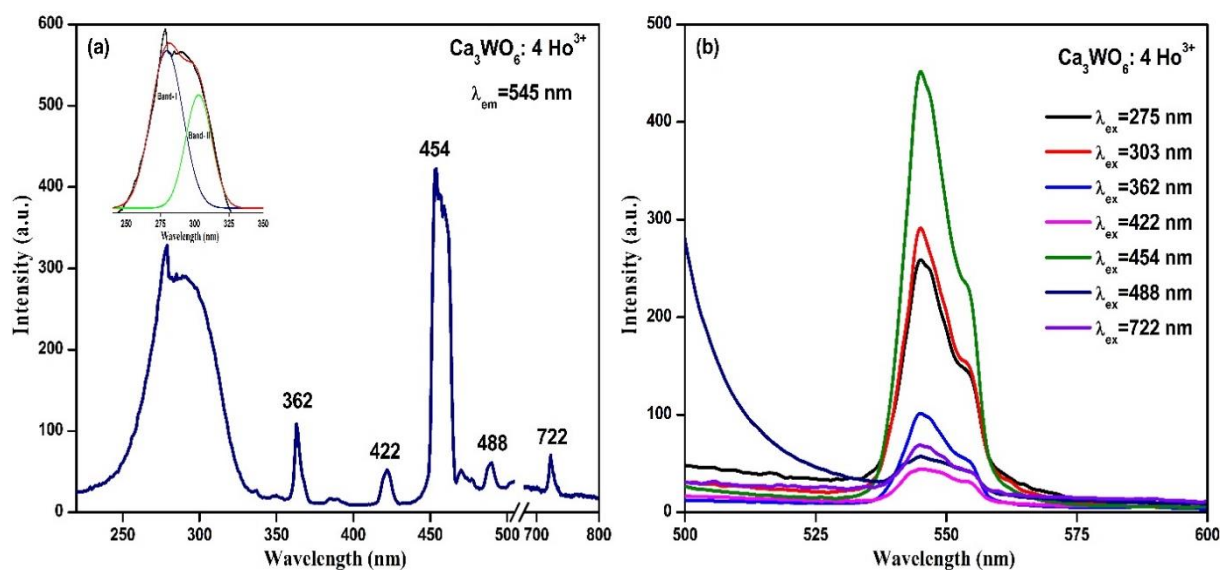


Figure 5.28. (a) PL excitation spectra of $\text{Ca}_3\text{WO}_6: 4 \text{ mol}\% \text{Ho}^{3+}$ (b) PL emission spectra of $\text{Ca}_3\text{WO}_6: 4 \text{ mol}\% \text{Ho}^{3+}$ phosphor.

Figure 5.28 (a) and (b) depicts the room temperature PL excitation and PL emission spectra of 4 mol% Ho^{3+} doped Ca_3WO_6 phosphor. In order to record the PL excitation, the emission wavelength of 545 nm, corresponds to predominant emission transition $^5\text{F}_4\text{-}^5\text{I}_8$ of Ho^{3+} was considered [51]. As Ho^{3+} consisted with large excitation states, the excitation spectrum was recorded in very broad wavelength range, starting from MUV (220 nm) to the NIR (800 nm) region. When monitored with 545 nm wavelength, large number of excitation peaks were detected at 275 nm, 303 nm, 362 nm, 422 nm, 454 nm, 488 nm, and 722 nm with dominating excitation wavelength of 454 nm. In the middle UV region of excitation (220-350 nm), a broad and intense excitation band is observed with absorption spike at 275 nm. Upon deconvolution of that region, we found two well-resolved bands centred at 275 nm and 303 nm, respectively. A spike of band-I centred at 275 nm is attributed to the charge transfer occurring between host and the activator. The charge transfer process is taking place from 2p orbital oxygen to the 4f orbital of the luminescent activator Ho^{3+} . Another absorption band centred at around 303 nm is resulted due to the charge transfer states of WO_6 octahedra of the host crystallites [52,53]. In addition to the charge transfer absorption bands, a very wide range of f-f transition excitations were detected within NUV to NIR region. The excitation peak in NUV region at 362 nm is attributed to $^5\text{I}_8\text{-}^3\text{H}_5\text{+}^3\text{H}_6$ characteristic transition of the doping ions. Whereas, the strongest excitation peak in terms of intensity located at 454 nm was attributed to $^5\text{I}_8\text{-}^3\text{H}_5\text{/}^5\text{F}_1$ transition of Ho^{3+} . Other two less intense peaks at 422 nm and 488 nm were ascribed to typical Ho^{3+} transitions occurring from $^5\text{I}_8\text{-}^3\text{K}_7$ and $^5\text{I}_8\text{-}^5\text{F}_3$, respectively [54]. A less intense excitation peak

appearing at higher wavelength side at 722 nm may be attributed to the host absorption. From the obtained excitation spectrum, it is concluded that the phosphor under study can be excited with a very broad range of excitations, from 275 nm to 722 nm.

Figure 5.28 (b) depicts the PL emission spectra of Ca_3WO_6 : 4 mol% Ho^{3+} phosphor recorded with various excitation wavelengths, mainly, 275 nm, 303 nm, 362 nm, 422 nm, 454 nm, 488 nm, and 722 nm. As the predominant transition of $\text{Ho}^{3+} {}^5\text{F}_4-{}^5\text{I}_8$ gives its emission peak at 545 nm, the emission spectra were recorded within 500 nm to 600 nm of wavelength range. Under all the given excitation wavelengths, a single peak Ho^{3+} emission at 545 nm with excellent PL intensity was observed. A single and most intense emission peak in emission spectra located at 545 nm is attributed to the ${}^5\text{S}_2/{}^5\text{F}_4-{}^5\text{I}_8$ basic characteristic transition of Ho^{3+} [55]. It should be mentioned, in addition to the down-conversion green emission, we also observed up-conversion green luminescence emission from the studied singly Ho^{3+} doped phosphor system when excited with 722 nm. When the phosphor under study was excited using 722 nm excitation wavelength, a very good green spectral emission was observed with emission peak 545 nm, which is characteristic holmium emission occurring due to ${}^5\text{S}_2/{}^5\text{F}_4-{}^5\text{I}_8$ transition.

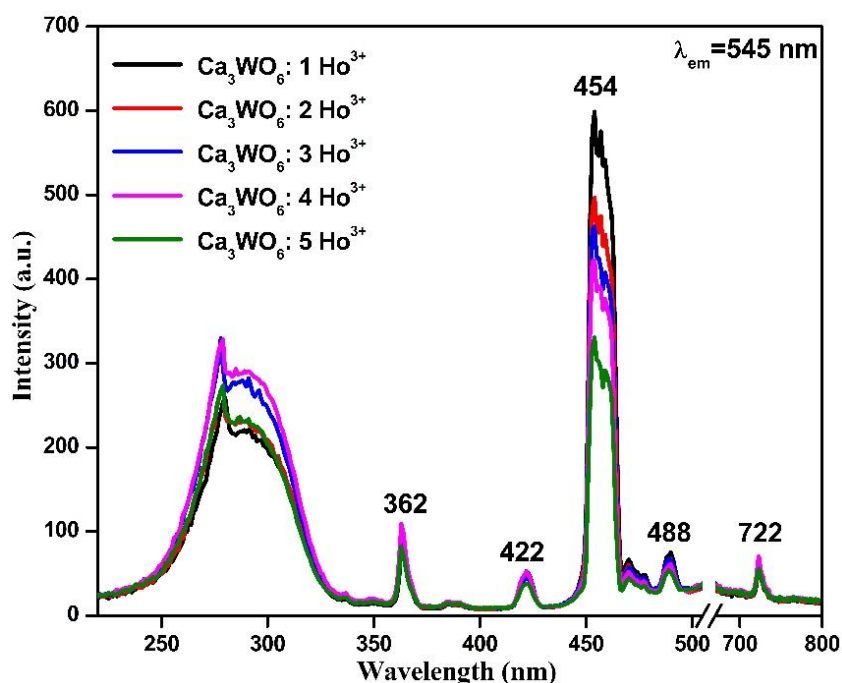


Figure 5.29. PL excitation spectra of Ca_3WO_6 : x mol% Ho^{3+} ($x=1-5$) phosphors recorded under 454 nm excitation wavelength.

Figure 5.29 depicts the PL excitation spectra of Ca_3WO_6 : x mol% Ho^{3+} ($x=1-5$) phosphors monitored with 545 nm emission wavelength. For the given emission wavelength, all the phosphors under study exhibited similar patterns of PL excitation, wherein the intensity

of PL excitation is slightly changes with varying concentrations. From the figure, it is interesting to note that the peaks located at 275 nm, 303 nm (WO_6 absorption band) 362 nm, and 722 nm exhibited maximum intensity for the doping concentration of 4 mol% of Ho^{3+} . Whereas, relatively intense peaks located at 422 nm, 454 nm and 488 nm exhibited maximum intensity for the doping concentration of 1 mol% of Ho^{3+} .

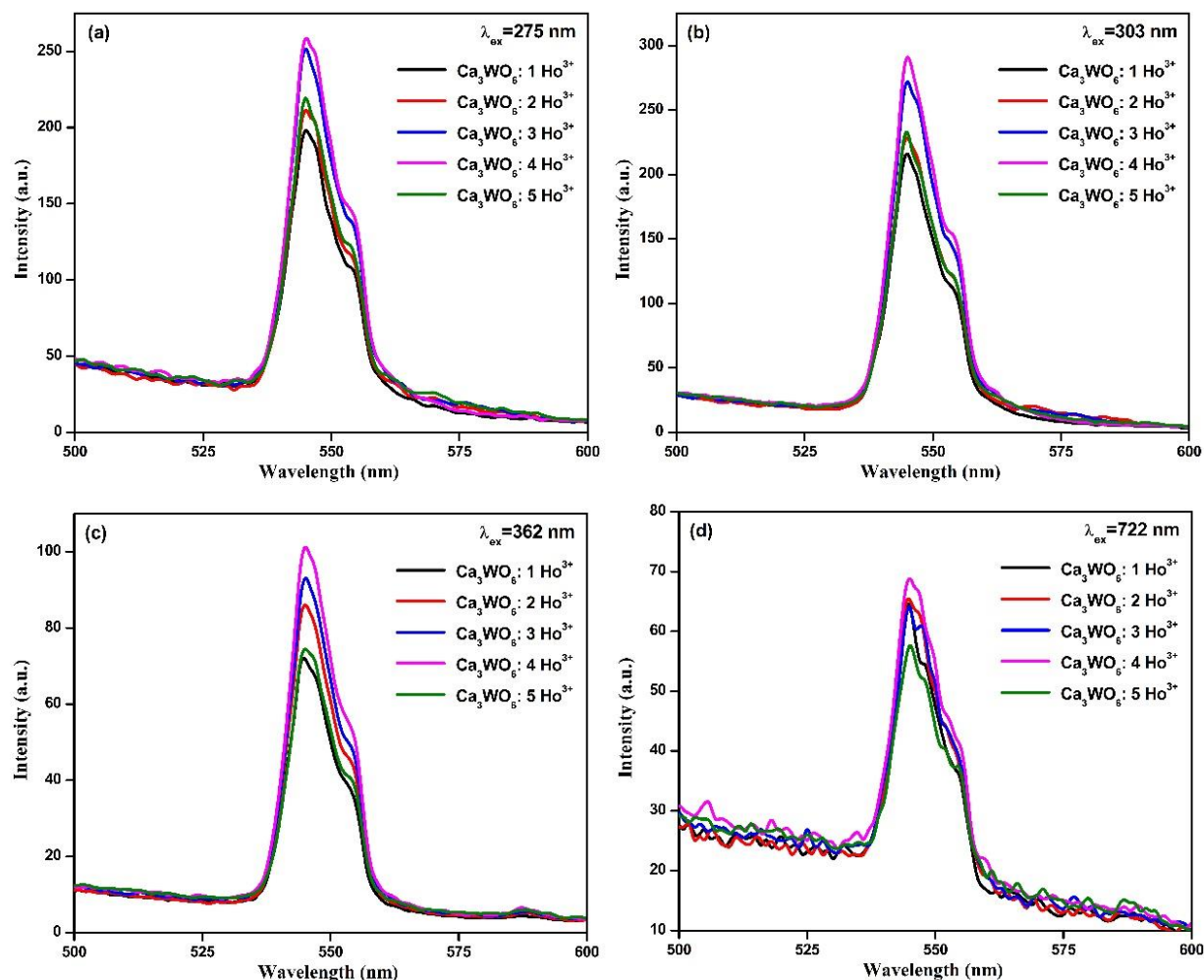


Figure 5.30. PL emission spectra of Ca_3WO_6 : x mol% Ho^{3+} ($x=1-5$) phosphors monitored with (a) 275 nm, (b) 303 nm, (c) 362 nm, and (d) 722 nm excitation wavelengths.

Figure 5.30 (a), (b), (c), and (d) depicts the PL emission spectra of Ca_3WO_6 : x mol% Ho^{3+} ($x=1-5$) phosphors recorded with 275 nm, 303 nm, 362 nm, and 722 nm excitation wavelengths. For all the mentioned excitations, all the phosphor under study shows single peaked PL emission at 545 nm of Ho^{3+} , which is results due to $^5\text{S}_2/5\text{F}_4-5\text{I}_8$ characteristic transition of Ho^{3+} . The intensity of PL emission was highly influenced by the holmium concentration. Under all four given excitations, the intensity of PL emission was raised with increasing Ho^{3+} concentration, and become maximum for 4 mol% of Ho^{3+} . Whereas for higher

doping, PL intensity is reduced because of the standard concentration quenching phenomenon [56,57]. Like PL emission spectra, the intensity of PL excitation was also found maximum for 4 mol% Ho^{3+} doped phosphors, at the excitation wavelengths of 275 nm, 303 nm, 362 nm, and 722 nm. For 5 mol% Ho^{3+} doping, intensity quenching of around 12 % was observed.

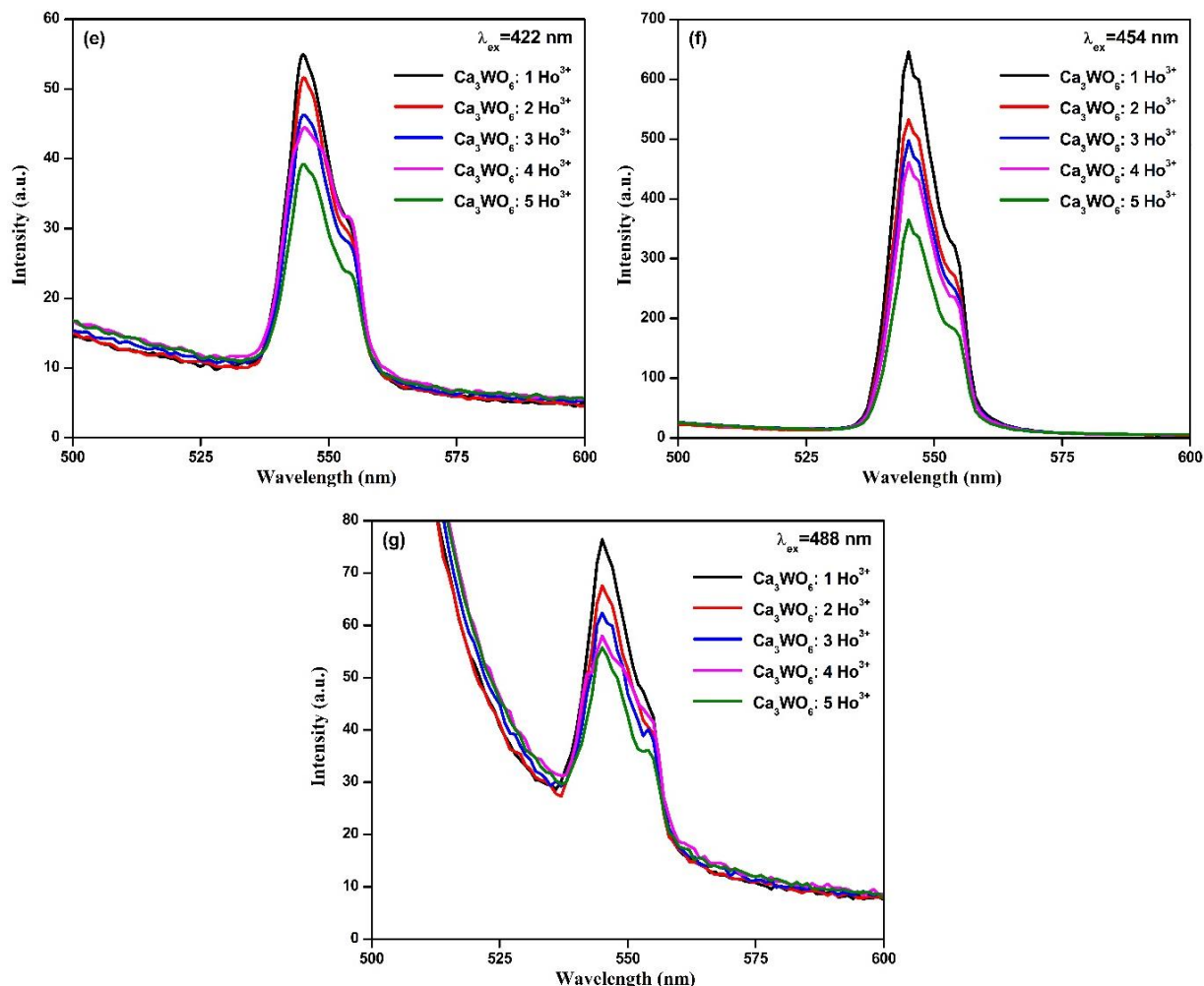


Figure 5.30. PL emission spectra of Ca_3WO_6 : x mol% Ho^{3+} (x=1-5) phosphors monitored with (e) 422 nm, (f) 454 nm, and (g) 488 nm excitation wavelengths.

Figure 5.30 (e), (f), and (g) depicts the PL emission spectra of Ca_3WO_6 : x mol% Ho^{3+} (x=1-5) phosphors recorded with 422 nm, 454 nm, and 488 nm excitation wavelengths. In comparison with all given excitations, the maximum intensity was obtained for 454 nm excitation. Herein, for all three mentioned excitations, the maximum intensity of PL emission was obtained from the phosphor doped with 1 mol% of Ho^{3+} . Under 422 nm, 454 nm, and 488 nm excitations, the PL intensity started decreasing with increasing doping concentration. Minimum intensity was obtained when the phosphor doped with 5 mol% of doping ions for all three excitations. In the studied phosphor system, quite interesting PL results we received.

Upon 275 nm, 303 nm, 362 nm, and 722 nm excitations, concentration quenching was occurred after 4 mol% of doping concentration. Whereas, for 422 nm, 454 nm, and 488 nm excitations, the maximum intensity was obtained for 1 mol% of Ho^{3+} doping, and for higher doping concentration, concentration quenching was observed [58]. The plot depicted in Figure 5.31 demonstrates the relation between the intensity of PL emission and Ho^{3+} concentration.

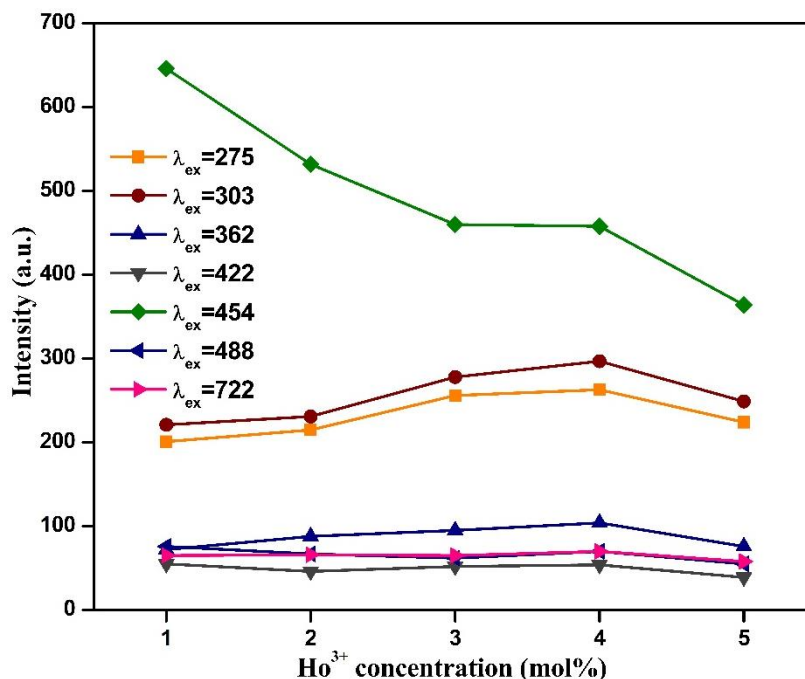


Figure 5.31. Plot of PL intensity vs. doping concentration.

A rise in the concentration of holmium ions leads to a reduction in the space between consecutive holmium ions within the host lattice. This closeness can possibly lead to the formation of pairs of Ho^{3+} or clusters of Ho^{3+} ions. As a result, reducing the distance between two consecutive Ho^{3+} ions be the cause of intensity quenching. This may explain using non-radiative energy transfer mechanism taking place between doping elements, such multipole-multipole interaction, radiation re-absorption, or exchange interaction. The mechanism of concentration quenching can be understood by the concept of critical distance (R_c) between doping elements. We calculated the R_c (formula 3.6) for two excitation wavelengths corresponding to two different quenching concentrations, mainly 275 nm (5 mol% quenching) and 454 nm (2 mol% quenching), and were found 13.48 Å and 18.30 Å, respectively. Obtained R_c under both applied excitations indicating multipole-multipole interaction as a cause of concentration quenching [59,60].

The intensity of PL emission is sensitive towards temperature in addition to the doping concentrations. To examine the phosphor performance (in the device) towards higher temperature, the PL emission of the 1 mol% Ho^{3+} doped phosphor under study was recorded at

different temperatures. The thermal stability of the phosphor material is an important aspect to investigate in order to implant it for its lighting device applications [61,62].

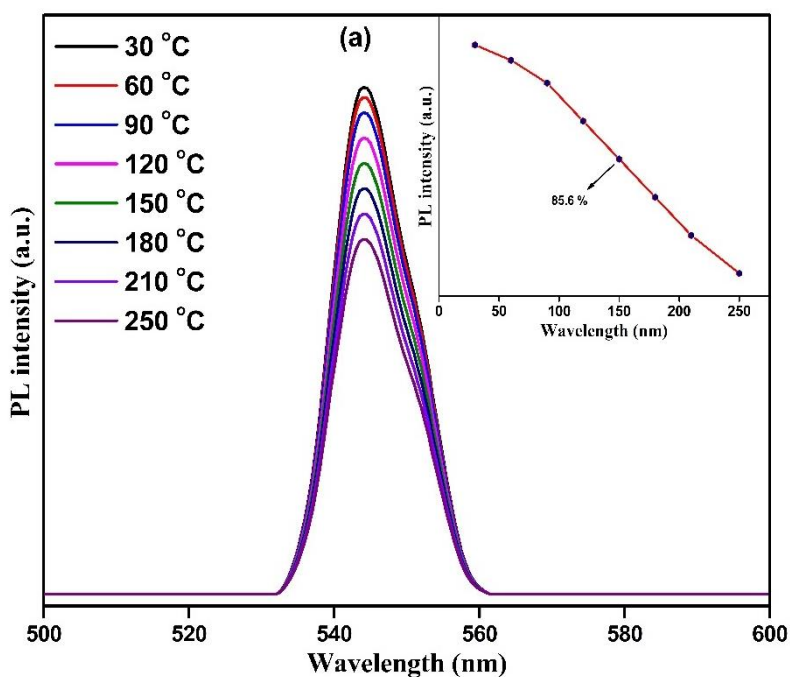


Figure 5.32. (a) Temperature dependent PL of $\text{Ca}_3\text{WO}_6:1 \text{ mol}\% \text{ Ho}^{3+}$ phosphor monitored with 454 nm.

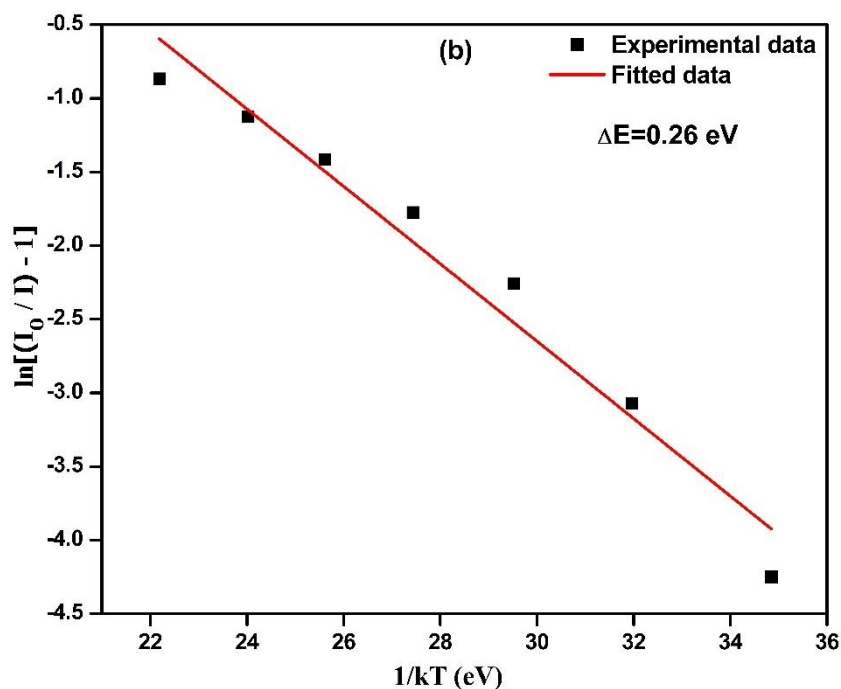


Figure 5.32. (b) Plot of $\ln[(I_0/I)-1]$ vs. $1/kT$ using plotted Arrhenius equation.

Herein, we examined the present phosphor system for their temperature-dependent PL (TDPL) by applying 454 nm excitation. The spectra were recorded from RT to 250 C° in

interval of 30 C°. Figure 5.32(a) depicts the TDPL spectra of 1 mol% Ho³⁺ doped phosphor under study recorded with 454 nm excitation. From the figure, it is observed, the raising in temperature leading to a reduction in PL intensity, however, the nature of the spectrum remained unaffected [63]. The reduction in PL intensity is primarily due to the thermal quenching phenomenon. Multiple mechanisms were responsible for thermal quenching, including thermally activated photoionization and multiphonon relaxation. The intensity of PL emission remained 85.6% at 150 C° and 71% at 250 C° when compared to the PL intensity observed at RT, shown in inset of figure 32(a). The excellent PL response of the phosphor under study at higher temperature is mainly ascribed to the rigid perovskite structure [64].

In addition, the Arrhenius model is applied to illustrate the thermal quenching, which describes the relation between temperature and their corresponding maximum PL intensities. Following the modified formula (equation 3.7) of the Arrhenius model for the calculation of activation energy (E_a) is utilized [65],

$$I(T) = \frac{I_0}{1 + c \exp(-E_a/kT)}$$

where, I(T) denote PL intensity at various temperatures, I₀ denotes the intensity of PL emission at room temperature. E_a stands for the activation energy, k denotes Boltzmann constant, whereas c is the constant. As per this relation, the plot of ln[(I₀/I)-1] as a function of 1/kT yield straight line. From Figure 32(b), the plot of ln[(I₀/I)-1] verses 1/kT, the data points yielded straight line. The slope of the straight line denotes the E_a. As a result, the E_a of 1 mol% Ho³⁺ doped phosphor is found to be 0.26 eV, when excited with 454 nm excitation. From the TDPL studies, it is concluded that the phosphor under study exhibited excellent thermal stability at blue-LED (454 nm) excitation, making it promising for its applications in warm WLEDs as a green component [66].

Moreover, we checked the thermal stability of the same phosphor by exciting it using 362 nm excitation wavelength for the purpose of using it for NUV excited LED phosphor. Figure 5.33(a) depicts the TDPL spectra of Ca₃WO₆:1 mol% Ho³⁺ phosphor recorded with 362 nm. From the figure, it is observed that the PL intensity decrease linearly with increasing temperature and remained 84.2 % at 150 C° and 65% at 250 C° when compared to the PL intensity recorded at RT. The observed value of PL intensity at 150 C° indicates good thermally stable luminescence upon LED operating temperature.

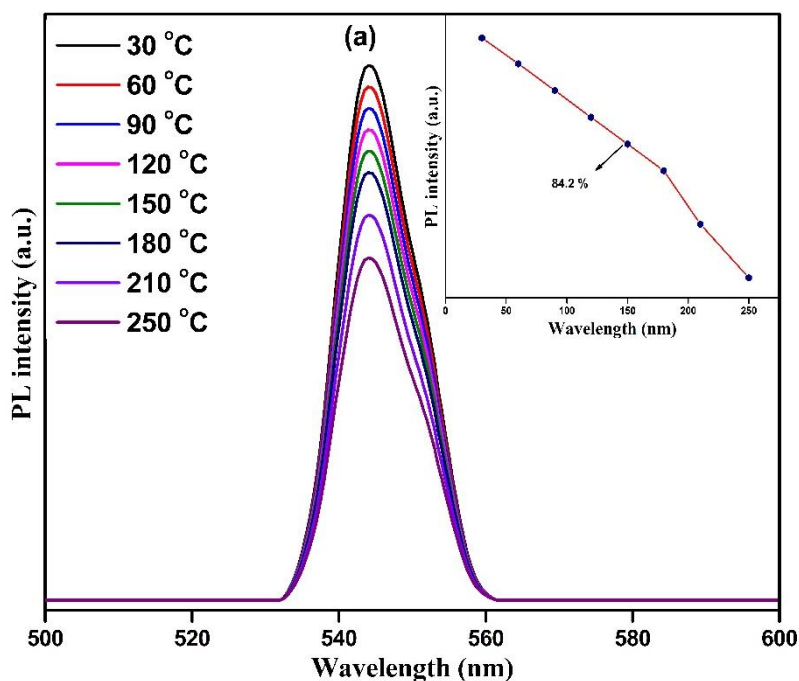


Figure 5.33. (a) Temperature dependent PL of $\text{Ca}_3\text{WO}_6:1 \text{ mol}\% \text{Ho}^{3+}$ phosphor monitored with 362 nm.

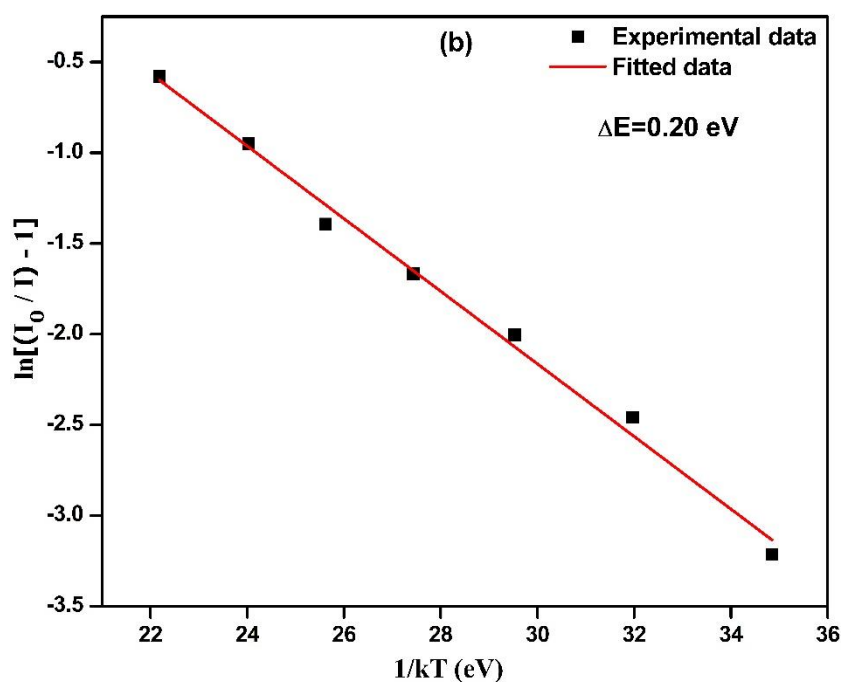


Figure 5.33. (b) Plot of $\ln[(I_0/I)-1]$ vs. $1/kT$ using plotted Arrhenius equation.

The activation energy was calculated via the plot between $\ln[(I_0/I)-1]$ and $1/kT$, shown in figure 5.33(b). The activation energy of the phosphor under study is found to be $E_a=0.20 \text{ eV}$ when it is excited with 362 nm. From the overall temperature dependent PL investigation, the

phosphor under study proven to be a very good green emitting phosphor for the WLEDs, whether it is excited with blue (454 nm) excitation or with NUV (362 nm) excitation.

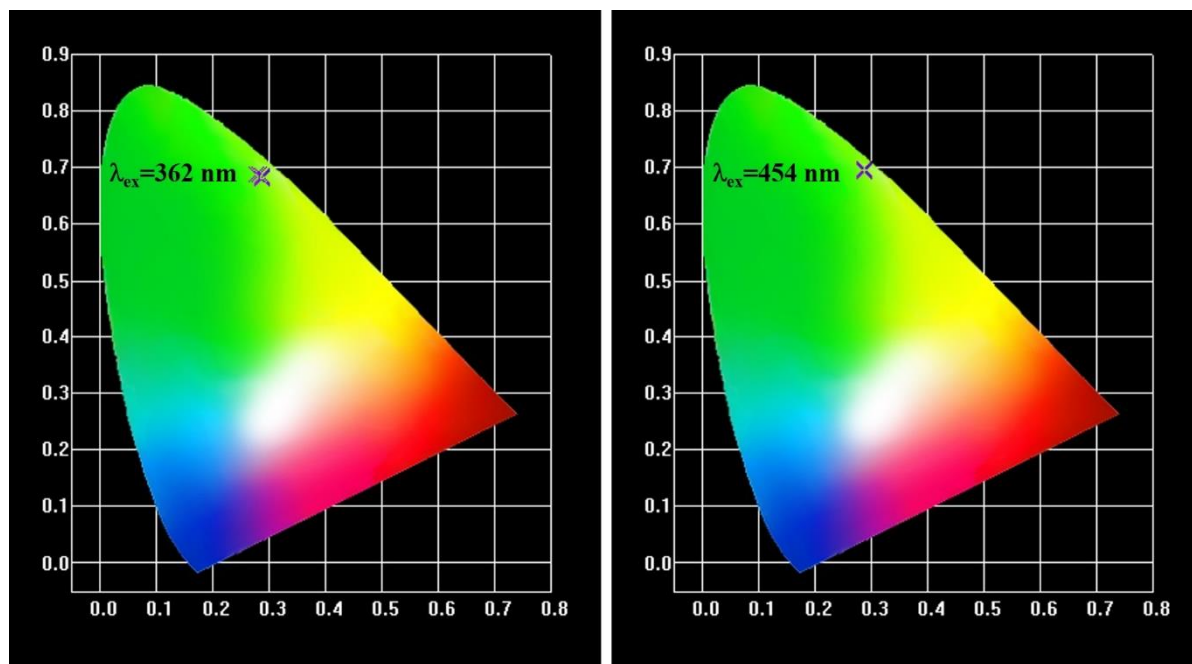


Figure 5.34. CIE diagram of Ho^{3+} doped Ca_3WO_6 phosphors for the excitations of 362 nm and 454 nm.

Moreover, to understand the performance of the studied series of Ca_3WO_6 phosphors, CIE color coordinates were computed and are presented in CIE diagram. Figure 5.34 presents the depiction of CIE points of Ho^{3+} doped Ca_3WO_6 phosphors. The CIE color coordinates were calculated for all phosphors for the excitation wavelengths of 362 nm and 454 nm. All the computed color coordinated are very near to the standard green color coordinates, and are lies in green spectral region, as shown in diagram [67,68]. A very fine color tunability was obtained upon different excitation wavelength from the same phosphor system. In addition, for the same excitation, color tunability was also observed from the phosphors having different Ho^{3+} concentration. By using the CIE points, the color purity and CCT of the all studied phosphors were computed using necessary formulas. Results obtained from the color coordinate study were tabulated in Table 5.7.

Sample	Excitation Wavelength	CIE co-ordinates		Color Purity (%)	CCT (K)
		X	Y		
Ca ₃ WO ₆ :1.0 % Ho ³⁺	362 nm	0.281	0.693	92.14	6248
	454 nm	0.287	0.698	93.25	6142
Ca ₃ WO ₆ :2.0 % Ho ³⁺	362 nm	0.301	0.676	87.75	5965
	454 nm	0.288	0.697	93	6136
Ca ₃ WO ₆ :3.0 % Ho ³⁺	362 nm	0.290	0.688	90.78	6119
	454 nm	0.288	0.696	92.75	6138
Ca ₃ WO ₆ :4.0 % Ho ³⁺	362 nm	0.285	0.692	91.82	6186
	454 nm	0.288	0.695	92.51	6240
Ca ₃ WO ₆ :5.0 % Ho ³⁺	362 nm	0.304	0.672	86.76	5920
	454 nm	0.288	0.693	92.02	6136

Table 5.7. CIE color coordinates determined parameters.

5.4.6 Thermoluminescence Studies

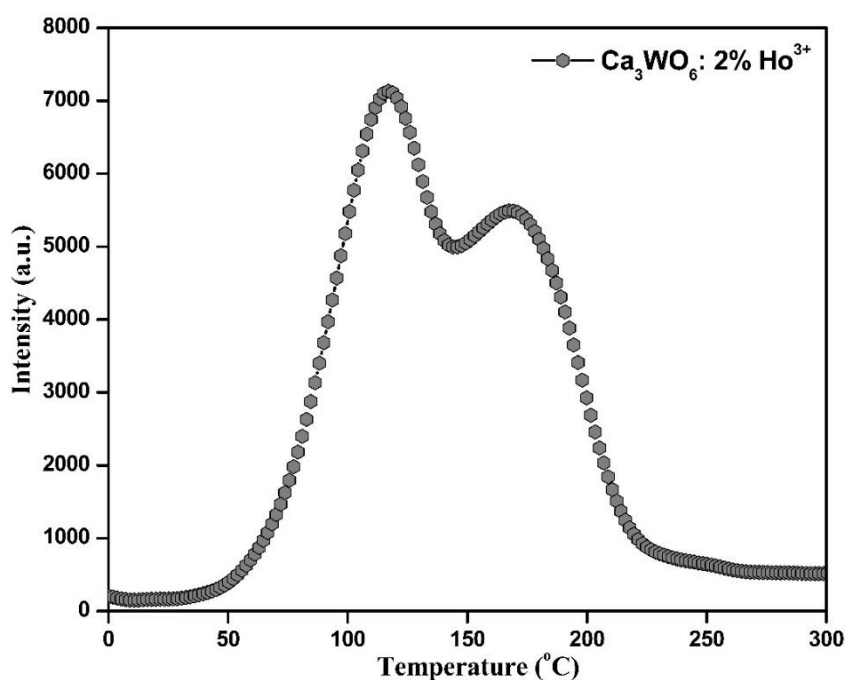


Figure 5.35. TL glow curve of Ca₃WO₆:2% Ho³⁺ phosphor irradiated with 50 Gy dose of beta rays.

First, we examined the thermoluminescence glow curve of Ca₃WO₆ double perovskite phosphor doped with 2 mol% of Ho³⁺. Among all the phosphors in this study doped with Ho³⁺, this sample exhibited the highest TL intensity when exposed to beta rays from a ⁹⁰Sr/⁹⁰Y beta source. Figure 5.35 demonstrates the TL glow curve of Ca₃WO₆:2% Ho³⁺ phosphor after being subjected to a 50 Gy beta dose. The TL measurements were conducted over a temperature range of 0 °C to 300 °C, with a constant heating rate of 4 °C/s. The studied phosphor Ca₃WO₆:2%

Ho^{3+} revealed remarkable TL glow upon beta irradiation. It displayed a prominent TL peak at approximately 117 °C, following by an additional peak at a higher temperature at around 170 °C. This acquired TL glow curve suggests the generation of two trap centres within the phosphor material when exposed to beta radiation. Notably, the shallower trap exhibited higher TL glow in comparison with the deeper trap generated towards higher temperature side.

To study the effect of varying Ho^{3+} doping level on the TL glow, the TL glow curves of Ca_3WO_6 phosphors activated with varied Ho^{3+} concentrations were recorded after 50 Gy dose of beta irradiation. The measurements of TL glow curves were taken at three different heating rates, primarily 2 °C/s, 4 °C/s, and 6 °C/s. The glow curves recorded with thee mentioned heating rates of the phosphors having varying Ho^{3+} doping concentration are depicted in figure 5.36 (a-c). Simultaneously, the effect of doping concentration and effect of heating rates can be visualized. The intensity of TL glow curves appears to be significantly influenced by the dopant concentration, as well as heating rate [69]. The nature of obtained glow curves seems slightly different, in terms of intensity. It should be mentioned that the undoped Ca_3WO_6 also exhibited good intense TL glow curve upon beta irradiation. The introduction of Ho^{3+} in the host lattice directly implies in small shifting in the most intense glow peak towards higher temperature side in comparison with the TL peak of undoped samples, when samples were heated at 4 °C/s. In case of 2 °C/s, and 6 °C/s, the shifting in glow peak position is less.

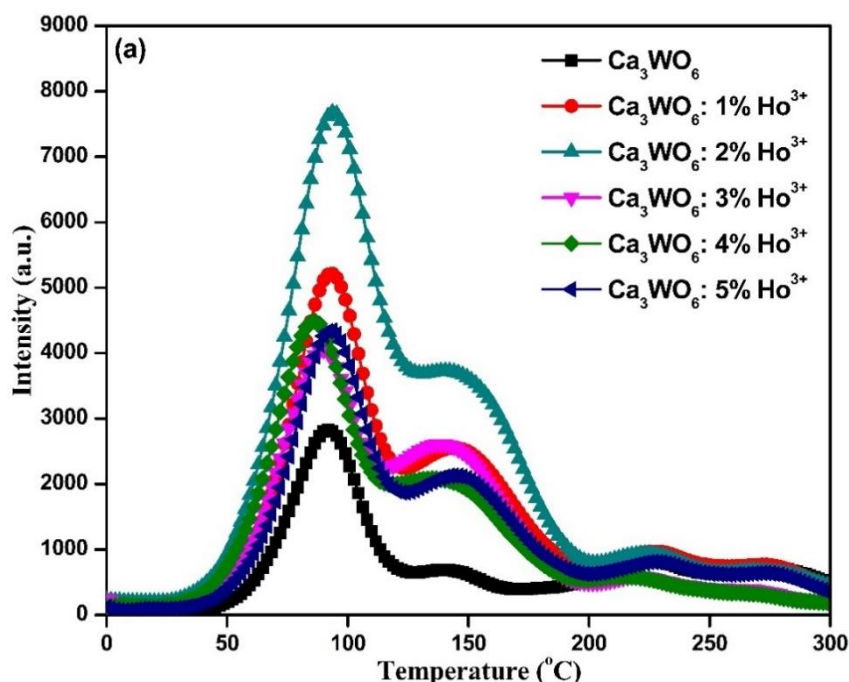


Figure 5.36. (a) TL glow curves of $\text{Ca}_3\text{WO}_6:x\% \text{Ho}^{3+}$ ($x=1-5$) phosphors after 50 Gy of beta irradiation, recorded at 2 °C/s heating rate.

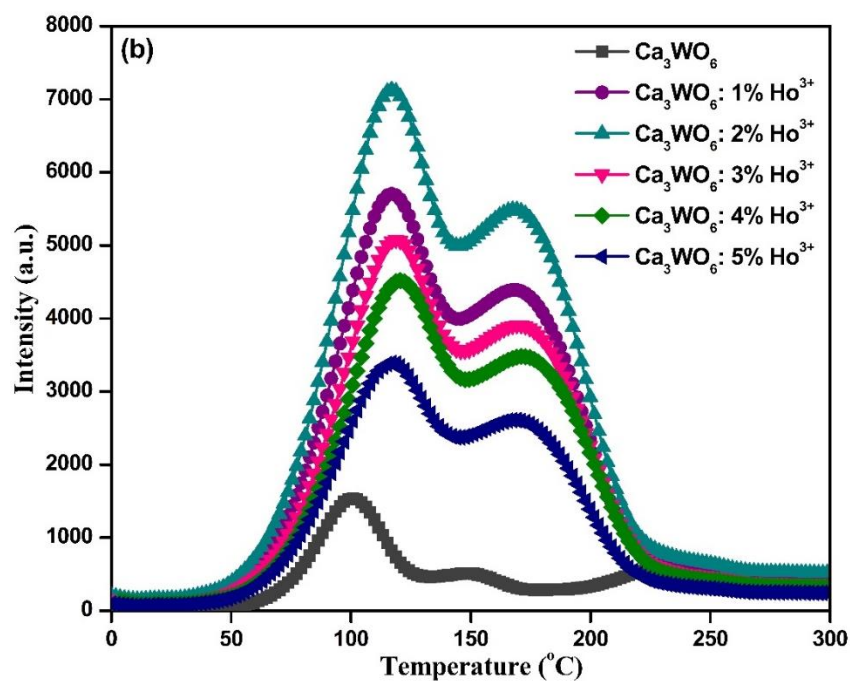


Figure 5.36. (b) TL glow curves of $\text{Ca}_3\text{WO}_6:x\% \text{Ho}^{3+}$ ($x=1-5$) phosphors after 50 Gy of beta irradiation, recorded at 4 °C/s heating rate.

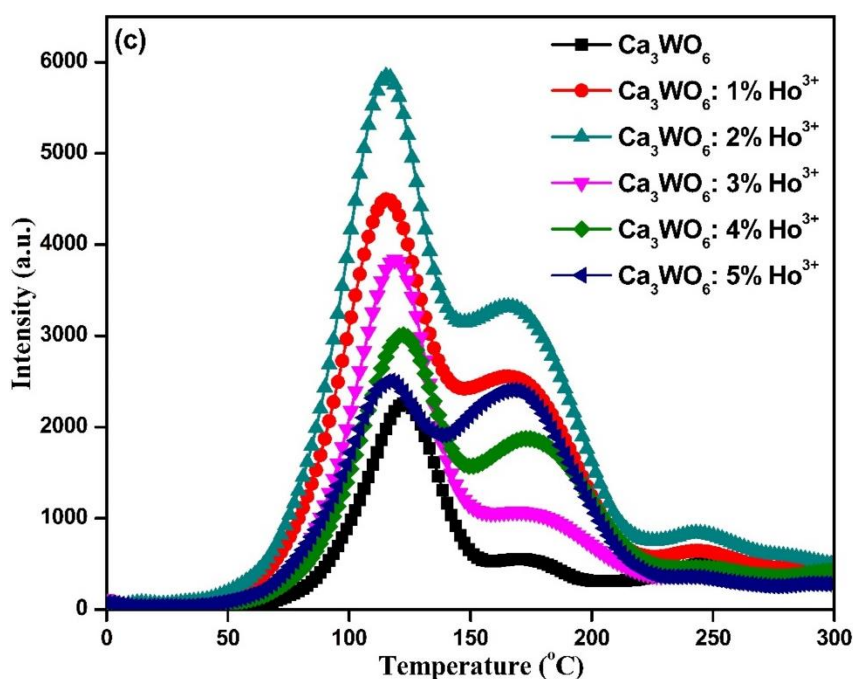


Figure 5.36. (c) TL glow curves of $\text{Ca}_3\text{WO}_6:x\% \text{Ho}^{3+}$ ($x=1-5$) phosphors after 50 Gy of beta irradiation, recorded at 6 °C/s heating rate.

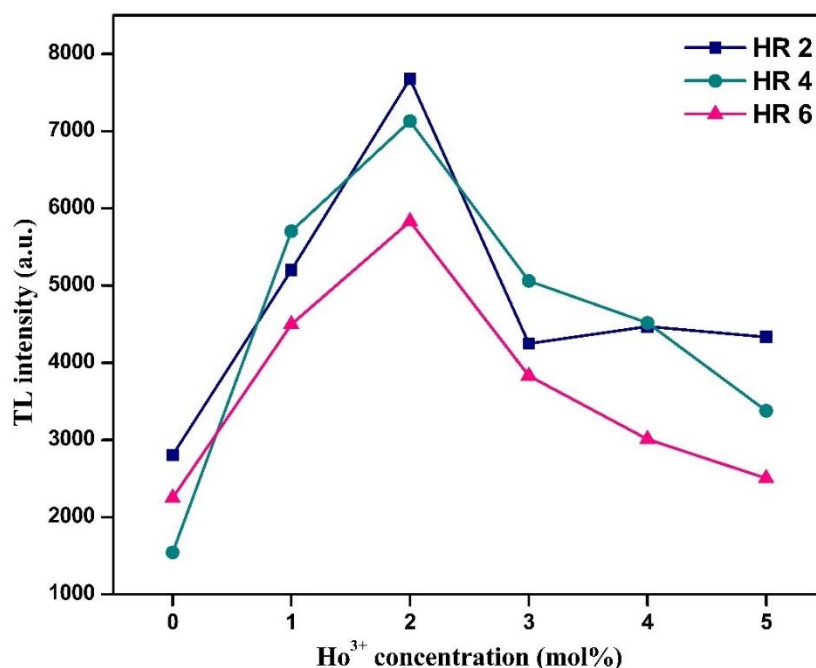


Figure 5.37. TL intensity response to different Ho^{3+} concentrations.

When Ho^{3+} concentration increase from 1 mol% to 2 mol%, the intensity of TL glow peak at 117 °C get enhanced, whereas, the nature of the glow curve remained unchanged. This observation remained true for all three applied heating rates (HR). Doping of 1 mol% notably increases the TL intensity, whereas increment in doping from 1 mol% to 2 mol% further increases the TL intensity. This observation indicates that the introduction of doping ions and increment in doping ions significantly increases the trapping centres, which were then observed in the glow curve intensity [70,71]. Maximum TL intensity was obtained from the phosphor doped with 2 mol% of Ho^{3+} ions. Further introduction Ho^{3+} resulting in concentration quenching. The TL response to varying doping concentration can be visualized by plotting TL intensity as a function of Ho^{3+} concentrations, and are depicted in Figure 5.37. Upon 3 mol% of Ho^{3+} doping resulting in intensity quenching. Excess amount of impurity in the host lattice resulting in closeness of two successive doping ions. In present case, 3 mol% doping of Ho^{3+} causes the TL intensity quenching, for any heating rate applied.

As we observed a good TL response from the phosphor under study for a heating rate of 4 °C/s, further TL studies were examined by recording the TL glow curves with a 4 °C/s heating rate.

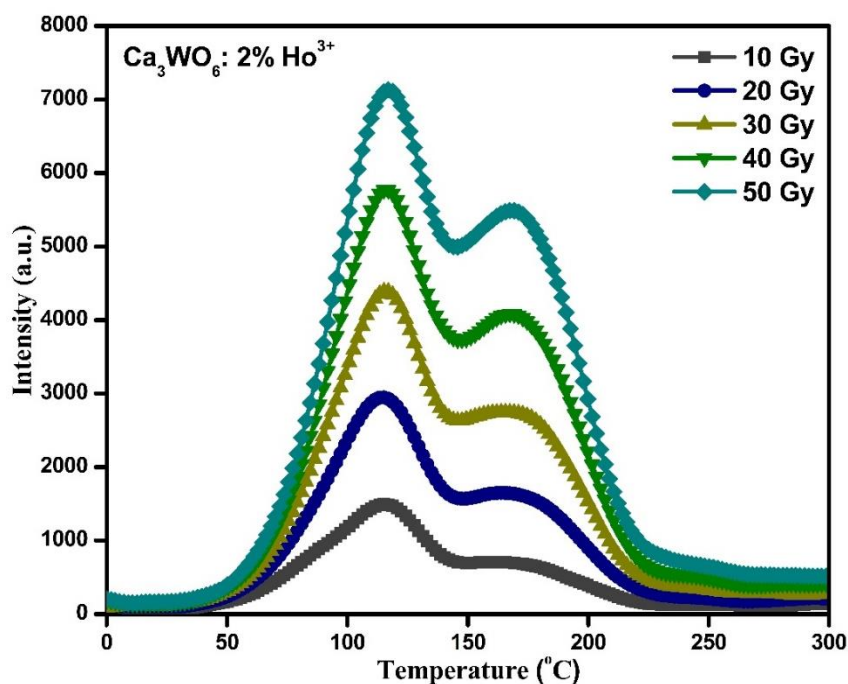


Figure 5.38. TL glow curves of $\text{Ca}_3\text{WO}_6:2\% \text{Ho}^{3+}$ phosphor at different doses of beta irradiation with a fixed heating rate of 4°C/s .

The intensity of TL glow of the phosphor materials can be highly affected by the exposure time of ionizing radiation in addition to the activator centres. Study on the TL dose response of the phosphor is crucial in order to apply it for the dosimetry purposes. Linear response of TL intensity with raising dose of ionizing radiation making phosphor potential for its applications in thermoluminescence dosimetry (TLD) [72]. To examine the dose response in Ca_3WO_6 phosphor series, all the Ca_3WO_6 phosphors under investigation were exposed to beta rays for wide range of exposure time. Figure 5.38 depicts the TL glow curves of the $\text{Ca}_3\text{WO}_6:2\% \text{Ho}^{3+}$ phosphor at mentioned beta doses, and were recorded with 4°C/s heating rate. The intensity of the TL glow peak tends to rise with increasing ionizing radiation dose. This result proposes that the number of trapping centres increased as the exposure time of beta irradiation increased [73]. As a result, the intensity of TL looks improved. The absorption of ionizing radiation is directly reflected in TL intensity counts. Nevertheless, we did not find any substantial changes in the shape of the glow curve or the peak position.

In order to examine the dose linearity from the present phosphor system, the plot of TL intensity as a function of beta dose was plotted, as illustrated in Figure 5.39. All the phosphor under study were irradiated with 10-50 Gy range of beta dose, and glow curves were recorded with 4°C/s heating rate. By considering the maximum intensity of the glow peak located at 117°C of all studied phosphors, the plot of TL intensity versus beta dose was drawn. The plot illustrates excellent linearity, indicative of a progressive growth in the generation of defect

centres with increasing beta dose. All Ho^{3+} doped as well as pure Ca_3WO_6 phosphors exhibited remarkable linear dose response with increasing beta dose. The outcomes from dose response study suggest that the studied phosphor series is a promising phosphor system for integrating into TL dosimeters [74].

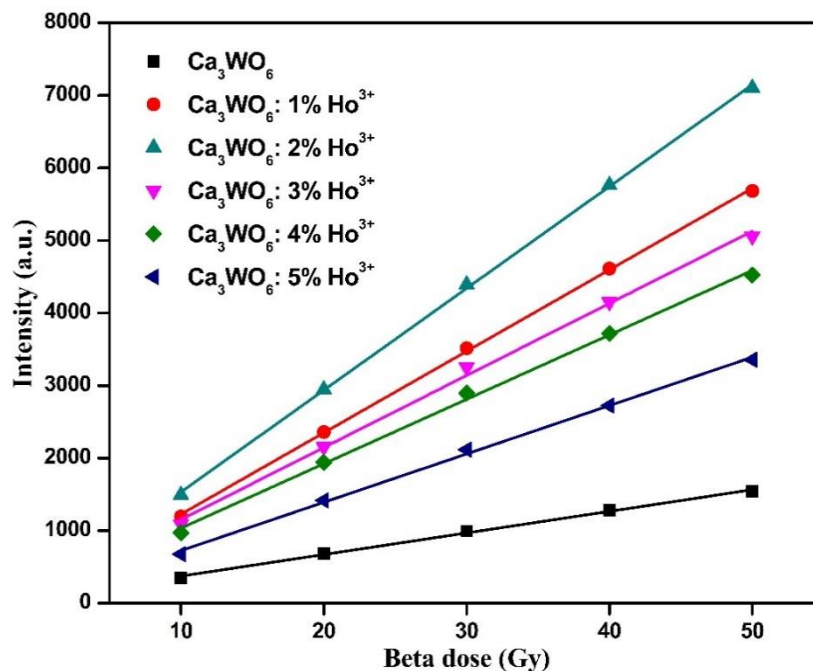


Figure 5.39. TL response of undoped and Ho^{3+} doped Ca_3WO_6 phosphors to beta irradiation.

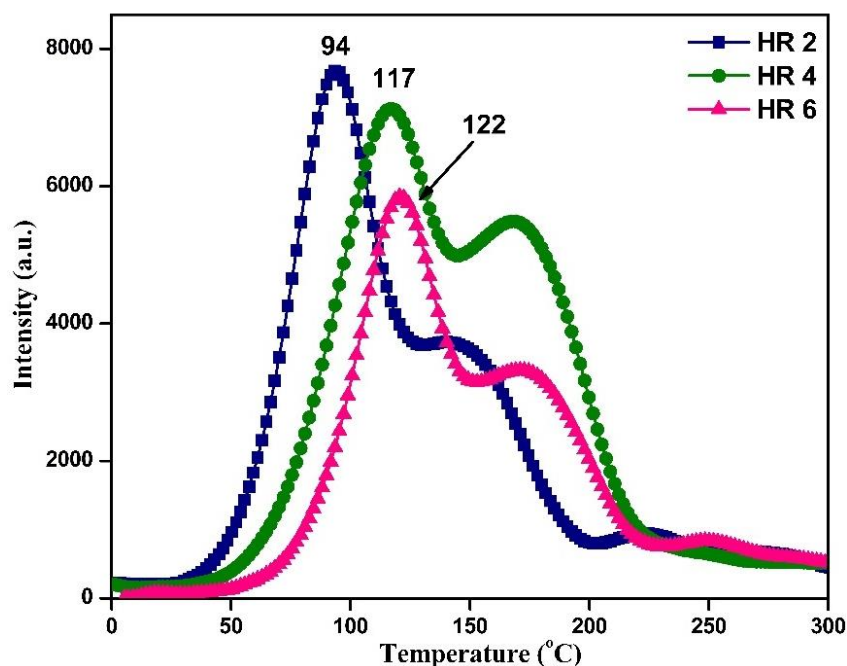


Figure 5.40. TL glow curves of Ca_3WO_6 :2% Ho^{3+} phosphor after irradiated with 50 Gy beta dose at heating rates of $2\text{ }^\circ\text{C s}^{-1}$, $4\text{ }^\circ\text{C s}^{-1}$, and $6\text{ }^\circ\text{C s}^{-1}$.

Another crucial parameter to study the dosimetry aspects of materials is the effect of heating rate (HR). As per the literature survey, the temperature of the glow peak is increases with higher HR, whereas, the TL intensity decreases with increasing HR [75,76]. In order to assess thermal quenching effect in the phosphor under study, the glow curves of $\text{Ca}_3\text{WO}_6:2\% \text{Ho}^{3+}$ phosphor were recorded between 0 °C to 300 °C with three different heating rates, mainly $2 \text{ }^\circ\text{C s}^{-1}$, $4 \text{ }^\circ\text{C s}^{-1}$, and $6 \text{ }^\circ\text{C s}^{-1}$. For all three applied heating rates, the glow curves were recorded after 50 Gy of beta dose, and results are depicted in figure 5.40.

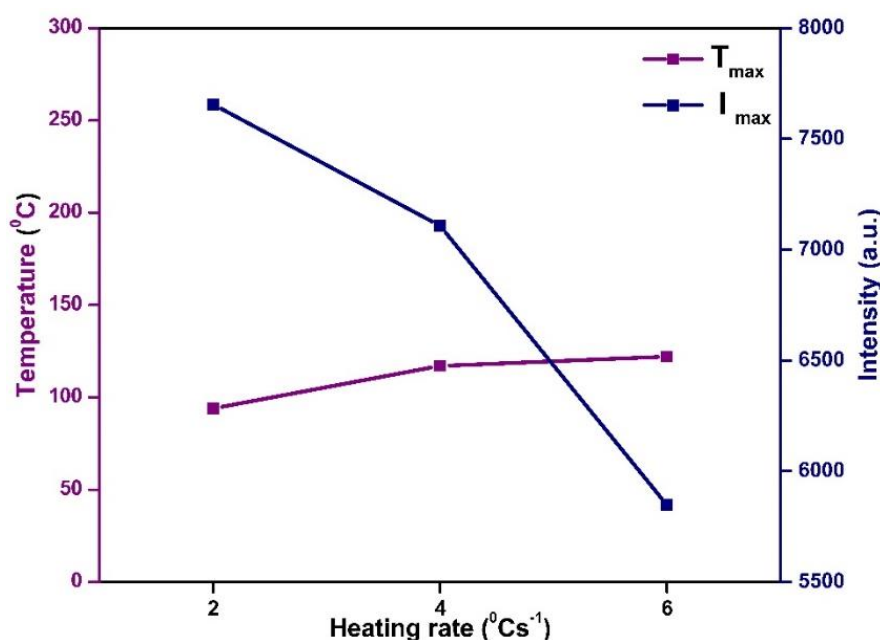


Figure 5.41. Plot of TL intensity and temperature as a function of HR.

As expected, the temperature value of the glow peak found to be shifted toward higher temperature with increasing heating rate. Whereas, the TL intensity counts found be reduced with raising HR. This behaviour confirms the appearances of one-trap-one-recombination (1T1R) model, which is the most fundamental TL model [77]. Figure 5.41 displays how the maximum peak temperature (T_m) values of the TL peak increase and the intensity (I_m) decreases due to the rising HR. From the obtained results from the HR studies, it is concluded that the thermal quenching found be extremely less from the phosphor under investigation [78].

For the trapping parameters calculation, the Chen's peak shape method (PSM) and GCD method were applied and subsequent trap parameters were calculated.

Figure 5.42 shows the deconvoluted TL glow curve of $\text{Ca}_3\text{WO}_6:2\% \text{Ho}^{3+}$ phosphor, the phosphor exhibited highest intensity among all studied. From the figure, it is observed that the glow curve consisted of three glow peaks with centre temperature of 117 °C, 158 °C, and 180 °C. With these deconvoluted peaks, first the geometrical factor ($\mu_g = \delta/\omega$) was computed in

order to examine the nature of glow curve. From the study, the second-order kinetics of all deconvoluted peaks was discovered [48]. Subsequently, the activation energy was computed using a common formula given by Chen, which was applicable for any order of kinetics available.

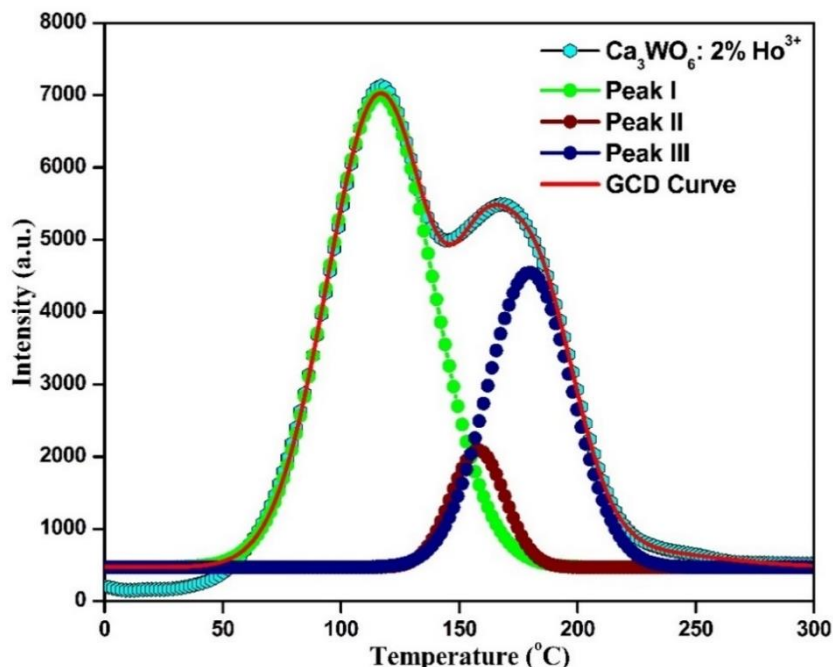


Figure 5.42. Deconvoluted TL glow curve of $\text{Ca}_3\text{WO}_6:2\% \text{Ho}^{3+}$ phosphor recorded after 50 Gy beta irradiation.

The activation energies for deconvoluted peaks of the glow curves obtained for each dose value are given in the Table 5.8. The calculated activation energies E_τ , E_δ and E_ω of $\text{Ca}_3\text{WO}_6:2\% \text{Ho}^{3+}$ phosphor at each given dose is ranging between 0.74-2.26 eV, 0.85-2.10 eV and 0.80-2.19 eV, respectively.

Moreover, by means of Kitis et al. equation of activation energy, the activation energy and frequency factor were also be determined for all the glow curves recorded with different doses of beta rays. As mentioned in PSM, the second-order kinetics of all three deconvoluted peaks were further supported by GCD. The computed activation energy via GCD technique ranges between 0.92 eV and 2.10 eV, which is very close to the activation energies determined using PSM. Trapping parameters calculated using GCD method are tabulated in Table 5.9.

Dose (Gy)		T_{max} (K)	μg	Activation Energy (eV)		
				E_{τ}	E_{δ}	E_{ω}
10	Peak-I	390	0.52	0.80±0.03	0.82±0.04	0.84±0.02
	Peak-II	431	0.50	2.08±0.19	2.10±0.21	2.10±0.13
	Peak-III	453	0.50	1.52±0.05	1.59±0.05	1.56±0.02
20	Peak-I	388	0.49	0.76±0.03	0.92±0.04	0.85±0.02
	Peak-II	431	0.52	2.26±0.19	2.10±0.20	2.19±0.10
	Peak-III	453	0.50	1.53±0.06	1.59±0.07	1.57±0.03
30	Peak-I	388	0.50	0.76±0.04	0.88±0.03	0.83±0.02
	Peak-II	431	0.52	2.26±0.07	2.10±0.13	2.19±0.06
	Peak-III	453	0.50	1.29±0.04	1.43±0.06	1.37±0.04
40	Peak-I	389	0.50	0.77±0.03	0.85±0.03	0.82±0.01
	Peak-II	431	0.52	1.92±0.14	1.82±0.17	1.87±0.08
	Peak-III	453	0.50	1.29±0.06	1.37±0.07	1.34±0.03
50	Peak-I	389	0.51	0.77±0.03	0.82±0.04	0.80±0.02
	Peak-II	431	0.50	1.92±0.14	2.10±0.14	2.02±0.07
	Peak-III	453	0.50	1.30±0.02	1.43±0.03	1.38±0.01

Table 5.8. Summary of TL kinetic parameters calculated by PSM.

Dose (Gy)		T_{max} (K)	Activation energy “ E_a ” (eV)	Order of kinetics “b”	Frequency factor “s” (s ⁻¹)
10	Peak-I	389	0.88±0.02	1.9	3.18×10^9
	Peak-II	431	2.01±0.20	1.9	1.20×10^{18}
	Peak-III	453	1.62±0.04	2.0	5.65×10^{11}
20	Peak-I	389	0.90±0.02	1.9	1.26×10^9
	Peak-II	431	1.92±0.20	1.9	9.13×10^{18}
	Peak-III	453	1.35±0.03	2.0	1.50×10^{10}
30	Peak-I	388	0.85±0.02	1.8	9.06×10^8
	Peak-II	431	2.10±0.15	1.9	6.17×10^{11}
	Peak-III	453	1.45±0.05	1.9	1.41×10^9
40	Peak-I	389	0.68±0.03	1.8	8.54×10^7
	Peak-II	431	1.91±0.17	1.9	1.41×10^{19}
	Peak-III	453	1.44±0.05	2.1	1.06×10^{11}
50	Peak-I	388	0.69±0.02	1.8	9.06×10^7
	Peak-II	430	2.10±0.15	2.0	2.53×10^{19}
	Peak-III	451	1.21±0.04	2.1	3.28×10^{11}

Table 5.9. Summary of TL kinetic parameters calculated by GCD.

References:

1. H. Zhang and H. Zhang, Special Issue: Rare earth luminescent materials, *Light Sci. Appl.* **11** (2022) 260.
2. V. Balaram, Rare earth elements: A review of applications, occurrence, exploration, analysis, recycling, and environmental impact, *Geoscience Frontiers* **10** (2019) 1285-1303.
3. J. Liu, Z. Wu, P. Wang et al., The effects of charge compensation on photoluminescence properties of a new green-emitting $\text{ZnB}_2\text{O}_4:\text{Tb}^{3+}$ phosphor, *Luminescence* **29** (2014) 868-871.
4. H. Wen, X. Lu, J. Liao et al., Preparation and luminescence properties of phosphors of rare earth complexes based on polyoxotungstates, *Mater. Res. Bull.* **68** (2015) 16-21.
5. I. Gupta, S. Singh, S. Bhagwan, and D. Singh, Rare earth (RE) doped phosphors and their emerging applications: A review, *Cera. Inter.* **47** (2021) 19282.
6. O. Golim, S. Huang, T. yang et al., Greenish-yellow emitting $\text{Ca}_9\text{MgLi}(\text{PO}_4)_7:\text{Dy}^{3+}$ phosphors-Photoluminescence and thermal stability, *J. Lumin.* **229** (2021) 117675.
7. S. Lee, S. Liu, T. Chan et al., Synthesis and Luminescence Properties of Novel Ce^{3+} - and Eu^{2+} -Doped Lanthanum Bromothiosilicate $\text{La}_3\text{Br}(\text{SiS}_4)_2$ Phosphors for White LEDs, *ACS Appl. Mater. Interfaces* **8** (2016) 9218-9229.
8. L. Dong, L. Zhang, Y. Jia et al., Site Occupation and Luminescence of Novel Orange-Red $\text{Ca}_3\text{M}_2\text{Ge}_3\text{O}_{12}:\text{Mn}^{2+}, \text{Mn}^{4+}$ (M = Al, Ga) Phosphors, *ACS Sustainable Chem. Eng.* **8** (2020) 3357-3366.
9. R. Hiramatsu, K. Ishida, F. Aiga et al., Tb^{3+} luminescence by energy transfer from Eu^{2+} in $(\text{Sr},\text{Ba})_2\text{SiO}_4$ phosphor, *J. Appl. Phys.* **106** (2009) 93513.
10. X. Liu, C. Li, Z. Quan et al., Tunable Luminescence Properties of $\text{CaIn}_2\text{O}_4:\text{Eu}^{3+}$ Phosphors, *J. Phys. Chem. C* **111** (2007) 16601-10067.
11. D. Mancebo, A. Becerro, A. Corral et al., Enhancing Luminescence and X-ray Absorption Capacity of $\text{Eu}^{3+}:\text{LaF}_3$ Nanoparticles by Bi^{3+} Codoping, *ACS Omega* **4** (2019) 765-774.
12. L. Rodrigues, H. Brito, J. Holsa et al., Discovery of the Persistent Luminescence Mechanism of $\text{CdSiO}_3:\text{Tb}^{3+}$, *J. Phys. Chem. C* **116** (2012) 11232-11240.
13. P. Xiong and M. Peng, Visible to near-infrared persistent luminescence from Tm^{3+} -doped two-dimensional layered perovskite Sr_2SnO_4 , *J. Mater. Chem. C* **7** (2019) 8303-8309.
14. J. Su, X. Zhang and X. Li, Hydrothermal synthesis and green up-conversion luminescence of Yb^{3+} and Ho^{3+} co-doped $\text{SrGd}_2(\text{WO}_4)_2(\text{MoO}_4)_2$ nanocrystal, *AIP Advances* **9** (2019) 125246.

15. X. Gao, D. Xu, J. Du et al., Research of optical absorption and luminescence spectra of double-perovskite calcium tungstate co-doped with $\text{Yb}^{3+}/\text{Ho}^{3+}$, *J. Mater. Sci: Mater. Electron.* **29** (2018) 1146-1152.
16. X. Yin, H. Wang, M. Xing et al., Upconversion luminescence of $\text{Y}_2\text{Ti}_2\text{O}_7:\text{Er}^{3+}$ under 1550 and 980 nm excitation, *J. Rare Earth* **35** (2017) 230-234.
17. Y. Patle, N. Brahme, D. Bisen et al., Study of Photoluminescence, Thermoluminescence, and Afterglow properties of Dy^{3+} doped $\text{Ba}_2\text{ZnSi}_2\text{O}_7$ phosphor, *Optik* **226** (2021) 165896.
18. G. Rosario, E. Cruz-Zaragoza, M. Hipolito et al., Synthesis and stimulated luminescence property of $\text{Zn}(\text{BO}_2)_2:\text{Tb}^{3+}$, *Appl. Radia. Isotop.* **127** (2017) 103-108.
19. L. Jiang, Y. Zhang, C. Li et al., Synthesis, photoluminescence, thermoluminescence and dosimetry properties of novel phosphor $\text{KSr}_4(\text{BO}_3)_3:\text{Ce}$, *J. Alloy. Comp.* **482** (2009) 313-316.
20. X. Zhao, J. Wang, L. Fan et al., Efficient red phosphor double-perovskite Ca_3WO_6 with A-site substitution of Eu^{3+} , *Dalton Trans.* **42** (2013) 13502-13508.
21. S. Zhang, Y. Hu, L. Chen et al., Photoluminescence properties and energy transfer of $\text{Ca}_3\text{WO}_6:\text{Sm}^{3+}$ co-doped Eu^{3+} , *Appl. Phys. A* **115** (2014) 1073-1080.
22. C. Wei, D. Xu, J. Li et al., Synthesis and luminescence properties of Eu^{3+} -doped a novel double perovskite Sr_2YTao_6 phosphor, *J. Mater. Sci: Mater. Electron.* **30** (2019) 2864-2871.
23. S. Pratibha, N. Dhananjaya and R. Lokesh, Investigations of enhanced luminescence properties of Sm^{3+} doped LaAlO_3 nanophosphors for field emission displays, *Mater. Res. Exp.* **6** (2020) 1250c7.
24. A. Zhang, Z. Sun, M. Jia et al., Sm^{3+} -doped niobate orange-red phosphors with a double-perovskite structure for plant cultivation and temperature sensing, *J. Alloy. Comp.* **889** (2021) 161671.
25. C. Limberkar, A. Patel, K. Patel et al., Anisotropic study of photo-bolometric effect in $\text{Sb}_{0.15}\text{Ge}_{0.85}\text{Se}$ ternary alloy at low temperature, *J. Alloy. Comp.* **846** (2020) 156391.
26. H. Najafi-Ashtiani, A. Bahari, S. Gholipour et al., Structural, optical and electrical properties of $\text{WO}_3\text{-Ag}$ nanocomposites for the electro-optical devices, *Appl. Phys. A* **124** (2018) 24.
27. H. Pang, X. Xiang, Z. Li et al., Hydrothermal synthesis and optical properties of hexagonal tungsten oxide nanocrystals assisted by ammonium tartrate, *Phys. Status Solidi A* **209** (2012) 537-544.

28. R. Balzer, V. Drago, W. Schreiner et al., Synthesis and Structure-Activity Relationship of a WO_3 Catalyst for the Total Oxidation of BTX, *J. Braz. Chem. Soc.* **25** (2014) 2026-2031.
29. O. Rezaee, H. Chenari and F. Ghodsi, Precipitation synthesis of tungsten oxide nanoparticles: X-ray line broadening analysis and photocatalytic efficiency study, *J. Sol-Gel Sci. Technol.* **80** (2016) 109-118.
30. A. Butt, S. Ejal, J. Baron et al, CaO NANOPARTICLES AS A POTENTIAL DRUG DELIVERY AGENT FOR BIOMEDICAL APPLICATIONS, *Dig. J. Nanomater. Biostruct.* **10** (2015) 799-809.
31. I. Koseva, P. Tzvetkov, P. ivsnov et al., Terbium-doped calcium germanate (Ca_2GeO_4) as a potential candidate for LED application, *J. Opt.* **49** (2020) 403-407.
32. S. Shimono, T. Izaki, N. Nagisa et al., Crystal structure, luminescence, and thermal stability of $\text{CsAlSi}_2\text{O}_6:\text{Tb}^{3+}$ phosphors with highly efficient green emission, *Maret. Res. Bull.* **143** (2021) 111441.
33. X. Wang, Z. Wang, S. Huang et al., Luminescence responses of $\text{CePO}_4:\text{Tb}$ monospheres toward vitamin C and permanganate, *Mater. Res. Bull.* **117** (2019) 28-34.
34. V. Singh, S. Watanabe, T. Rao et al., Luminescence and defect centres in Tb^{3+} doped $\text{LaMgAl}_{11}\text{O}_{19}$ phosphors, *Solid State Sci.* **12** (2012) 1981-1987.
35. V. Dubey, R. Tamarkar, R. Chanrakar et al., Effect of Tb^{3+} ion concentration on photoluminescence and thermoluminescence studies of $\text{Y}_4\text{Al}_2\text{O}_9$ phosphor, *Optik* **226** (2021) 165926.
36. B. Wang, Q. Ren, O. Hai et al., Luminescence properties and energy transfer in Tb^{3+} and Eu^{3+} co-doped $\text{Ba}_2\text{P}_2\text{O}_7$ phosphors, *RSC Adv.* **7** (2017) 15222-15227.
37. A. Kadam, S. Dhoble, G. Mishra et al., Combustion assisted spectroscopic investigation of Dy^{3+} activated SrYAl_3O_7 phosphor for LED and TLD applications, *J. Mol. Struct.* **1223** (2021) 130150.
38. C. Wang, Y. Jin, Y. Lv et al., A bifunctional phosphor $\text{Sr}_3\text{Sn}_2\text{O}_7:\text{Eu}^{3+}$: Red luminescence and photochromism properties, *J. Lumin.* **192** (2017) 337-342.
39. L. Wang, X. Yang, Q. Zhang et al., Luminescence properties of $\text{La}_2\text{O}_2\text{S}:\text{Tb}^{3+}$ phosphors and phosphor-embedded polymethylmethacrylate films, *Mater. Des.* **125** (2017) 100-108.
40. D. Taikar, Study of photoluminescence of Tb^{3+} doped Sr_2CeO_4 phosphor for UV LED application, *Mater. Today Proceed.* **29** (2020) 901-904.
41. H. Loksha and M. Chithambo, A combined study of the thermoluminescence and electron paramagnetic resonance of point defects in $\text{ZrO}_2:\text{Er}^{3+}$, *Radia. Phys. Chem.* **172** (2020) 108767.

42. A. D'Souza, K. Sharmila, M. Sayyed et al., Gamma ray shielding and thermoluminescence investigation of bismuth added heavy metal oxide glasses, *Radia. Phys. Chem.* **188** (2021) 109598.
43. K. Gavhane, M. Bhandane, A. Bhoir et al., T_m - T_{stop} analysis and dosimetric properties of Ce doped BaB_4O_7 phosphor, *J. Alloy. Comp.* **817** 152805.
44. M. Gowri, G. Darshan, Y. Naik et al., Phase dependent photoluminescence and thermoluminescence properties of $Y_2SiO_5:Sm^{3+}$ nanophosphors and its advanced forensic applications, *J. Alloy. Comp.* **96** (2019) 109282.
45. N. Patel, V. Verma, D. Modi et al., Thermoluminescence kinetic features of Eu^{3+} doped strontium pyrophosphate after beta irradiation, *RSC Adv.* **6** (2016) 77622-77628.
46. P. Gonzalez, D. Mendoza-Anaya, O. Avila et al., Synthesis, characterization and thermoluminescence properties of MgB_4O_7 phosphor co-doped with Tm and Dy, *Appl. Radia. Isotop.* **200** (2023) 110975.
47. A. Kumar, A. Kumar, R. Dogra et al., Investigation of thermoluminescence and kinetic parameters of gamma ray exposed $LiF: Sm^{3+}, Eu^{3+}$ nanophosphors for dosimetric applications, *Cera. Inter.* **44** (2018) 15535-15541.
48. T. Gavrilovic, K. Laganovska, A. Zolotarjovs et al., High resolution luminescence spectroscopy and thermoluminescence of different size $LaPO_4:Eu^{3+}$ nanoparticles *Opt. Mater.* **82** (2018) 39.
49. S. Chaki, M. Chaudhary, and M. Deshpande, Effect of indium and antimony doping in SnS single crystals, *Mater. Res. Bull.* **63** (2015) 173-180.
50. R. Sagheer, M. Khalil, V. Abbas et al., Effect of Mg doping on structural, morphological, optical and thermal properties of ZnO nanoparticles, *Optik* **200** (2020) 163428.
51. V. Shanbhag, S. Prashantha, R. Naik., et al., Photoluminescence properties of $CaTiO_3:Ho^{3+}$ nanophosphors for light emitting display applications, *Mater. Today Proceed.* **46** (2021) 5953-5957.
52. J. Malleshappa, H. Nagabhushana, D. Kavyashree et al., Shape tailored green synthesis of $CeO_2:Ho^{3+}$ nanopowders, its structural, photoluminescence and gamma radiation sensing properties, *Spectrochemi. Acta A: Mol. Biomole. Spectro.* **145** (2015) 63-75.
53. X. Zhang, Z. Li, H. Zhang et al., Luminescence properties of $Sr_2ZnWO_6:Eu^{3+}$ phosphors, *J. Alloy. Comp.* **469** (2009) L6-L9.
54. V. Singh, C. Annapurna Devi, S. Kaur et al., Optical properties of $Sr_2La_8(SiO_4)_6O_2$ doped with Ho^{3+} phosphor, *Optik* **242** (2021) 167268.

55. H. Premkumar, B. Ravikumar, D. Sunitha et al., Investigation of structural and luminescence properties of Ho^{3+} doped YAlO_3 nanophosphors synthesized through solution combustion route, *Spectrochemi. Acta A: Mol. Biomole. Spectro.* **115** (2013) 234-243.
56. V. Havasi, G. Sipos, Z. Konya et al., Luminescence and color properties of Ho^{3+} co-activated $\text{Sr}_4\text{Al}_{14}\text{O}_{25}:\text{Eu}^{2+}, \text{Dy}^{3+}$ phosphors, *J. Lumin.* **220** (2020) 116980.
57. T. Rao, C. Satya Kaml, T. Samuel et al., Color tunable luminescence from $\text{LaAlO}_3:\text{Bi}^{3+}, \text{Ho}^{3+}$ doped phosphors for field emission displays, *J. Mater. Sci: Mater. Electron.* **29** (2018) 1011-1017.
58. M. Tataseno, A. Ryadun, Z. Orazov et al., The Concentration Quenching of Photoluminescence and the Quantum Yield in $(\text{Y}_{1-x}\text{Pr}_x)_2\text{O}_2\text{Se}$ Solid Solutions, *Inorg. Mater.* **57** (2021) 830-834.
59. L. Melato, O. Ntwaeabrwa, R. Kroon et al., Effect of Ho^{3+} concentration on the structure, morphology and optical properties of $\text{Ba}_{0.5}\text{Mg}_{0.5}\text{Al}_2\text{O}_4$ nanophosphor, *J. Mol. Struct.* **1176** (2019) 217-225.
60. M. Ilhan, R. Samur, H. Demirer et al., Photoluminescence and concentration quenching of Pr^{3+} doped BaTa_2O_6 phosphor, *Metalurgia* **54** (2015) 407-410.
61. V. Kumar, S. Som, S. Dutta et al., Influence of Ho^{3+} doping on the temperature sensing behavior of $\text{Er}^{3+}-\text{Yb}^{3+}$ doped $\text{La}_2\text{CaZnO}_5$ phosphor, *RSC Adv.* **6** (2016) 84914-84925.
62. J. Li, X. Yuan, P. Jing et al., Temperature-dependent photoluminescence of inorganic perovskite nanocrystal films, *RSC Adv.* **6** (2016) 78311-78316.
63. M. Aida and M. Hjiri, Temperature-dependent photoluminescence of Li-doped ZnO, *J. Mater. Sci: Mater. Electron.* **31** (2020) 10521-10530.
64. N. Degda, N. Patel, V. Verma et al., Europium doped Sr_2YNbO_6 double perovskite phosphor for photoluminescence and thermoluminescence properties, *Luminescence* **38** (2023) 176-187.
65. Y. Chen, Y. Shen, L. Zhou et al., Temperature-dependent luminescence of $\text{Bi}^{3+}, \text{Eu}^{3+}$ co-activated $\text{La}_2\text{MgGeO}_6$ phosphor for dual-mode optical thermometry, *J. Lumin.* **249** (2022) 118995.
66. H. Guo, B. Devakumar, R. Vijayakumar et al., A novel Sm^{3+} singly doped $\text{LiCa}_3\text{ZnV}_3\text{O}_{12}$ phosphor: a potential luminescent material for multifunctional applications, *RSC Adv.* **8** (2018) 33403-33413.

67. V. Shanbhag, S. Prashantha, R. R. Naik et al., Photoluminescence properties of $\text{CaTiO}_3:\text{Ho}^{3+}$ nanophosphors for light emitting display applications, *Mater. Today Proceed.* **46** (2021) 5953-5957.
68. A. Dwivedi, A. Roy and S. Rai, Photoluminescence behavior of rare earth doped self-activated phosphors (i.e. niobate and vanadate) and their applications, *RSC Adv.* **13** (2023) 16260.
69. P. Kaur, A. Kaur, S. Singh et al., Investigation on structural and thermoluminescence properties of Ho^{3+} doped SrB_4O_7 phosphor for dosimetry applications, *J. Mol. Struct.* **1248** (2022) 131500.
70. A. Kadam, G. Mishra and S. Dhoble, Thermoluminescence study of Eu^{3+} doped $\text{Na}_2\text{Sr}_2\text{Al}_2\text{PO}_4\text{Cl}_9$ phosphor via doping of singly, doubly and triply ionized ions, *Cera. Inter.* **46** (2020) 132-155.
71. S. Bargat, Y. Parauha, G. Mishra et al., Thermoluminescence study of $\text{CaNa}_2(\text{SO}_4)_2$ phosphor doped with Eu^{3+} and synthesized by combustion method, *Luminescence* **36** (2020) 1862-1868.
72. K. V. R. Murthy, A. Sai Prasad, and M. Ramalingeshwar, Luminescence Characteristics of Eu and Tb doped YGdBO_3 Phosphor, *Phys. Proced.* **29** (2012) 70-75.
73. M. Sen, R. Shukla, N. Pathak et al., Development of $\text{LiMgBO}_3:\text{Tb}^{3+}$ as a new generation material for thermoluminescence based personnel neutron dosimetry, *Mater. Adv.* **2** (2021) 3405.
74. A. Oza, V. Ojha, S. Dhale et al., Photoluminescence and thermoluminescence in Dy^{3+} -, Ce^{3+} -, and Tb^{3+} -activated MgB_4O_7 phosphor for dosimetry application, *Luminescence* **37** (2022) 1563-1574.
75. T. Verma and S. Agrawal, Effect of Heating Rate on Thermoluminescence Glow Curves of Rare Earth Doped Y_2O_3 Phosphor, *Mater. Today Proceed.* **3** (2016) 4232-4235.
76. Y. Alajlani, M. Oglakci, U. Kaynar et al., Thermoluminescence study and evaluation of trapping parameters of samarium doped barium silicate phosphor, *J. Asian Ceram. Soc.* **9** (2021) 291-303.
77. J. Hakami, M. Sonsuz, u. Kaynar et al., Thermoluminescence glow curve analysis of $\text{Ca}_3\text{Y}_2\text{B}_4\text{O}_{12}$ phosphor prepared using combustion method, *Appl. Radia. Isotop.* **186** (2022) 110299.
78. J. Hakami, M. Oglakci, Z. Portakal-Ucar et al., Samarium doped $\text{Ca}_3\text{Y}_2\text{B}_4\text{O}_{12}$ phosphor prepared by combustion method: Anomalous heating rate effect, dosimetric features, and TL kinetic analyses, *J. Lumin.* **251** (2022) 119200.